



UNIVERSITÀ DEGLI STUDI DI PADOVA

DIPARTIMENTO DI TECNICA E GESTIONE DEI
SISTEMI INDUSTRIALI

Tesi di Laurea Magistrale in Ingegneria Gestionale

Anodizing of an AlSi10Mg alloy produced by
selective laser melting

Relatore: Ch.mo Prof. Giulio Timelli
Correlatore: Prof.ssa Caterina Zanella
Dr Baiwei Zhu

Laureando: Gaia Falcone
Matricola: 1185146

Vorrei dedicare questo spazio a chi, con dedizione e pazienza, ha contribuito alla realizzazione di questo elaborato.

Un ringraziamento particolare va al mio relatore Ch.mo Professor Timelli Giulio che mi ha seguito, con la sua infinita disponibilità, in ogni step della realizzazione dell'elaborato a partire dalla scelta dell'argomento.

Grazie anche a i miei correlatori la Professoressa Zanella Caterina e il Dottor Zhu Baiwei per i preziosi consigli e per aver contribuito alla formazione necessaria per affrontare anche la parte sperimentale

Un ringraziamento speciale va anche a Dr.ssa Donya Ahmadkhaniha e Mr. Jürgen Bloom che mi hanno aiutato a condurre le ricerche, oggetto del mio elaborato, e mi hanno sostenuto anche a livello morale durante questo percorso.

Infine ringrazio i miei amici, i miei colleghi di università e quelli di lavoro che hanno condiviso con me fatiche e gioie di questi anni passati insieme.

“Ma non sarò neanche tanto stupido

Da credere che il mondo

Possa crescere se non parto da me”

Summary

This study aims to evaluate the response of AlSi10Mg alloys made by selective laser melting (SLM) technology to the anodizing process.

The anodising of SLM samples is performed in a bath of H₂SO₄ at a constant voltage of 30 V for 45 mins at 22±1°C.

Microstructural analyses under an optical (LOM) and electron microscope (SEM) were conducted to characterise the thickness and morphology of the anodic layer. Micro-hardness tests and resistance to wear and corrosion were carried out to study the mechanical properties of the oxide layer. The outcomes demonstrate that the anodic layer has a thickness of 4±0.1µm, 4.2±0.1 GPa of hardness and a wear rate of 0.98×10⁻⁵ mm³/(N mm) with 0.38±0.2µm of roughness. Furthermore, after 12 hours of the immersion of the anodized sample in 3% of NaCl solution, the corrosion attack penetrated the oxide layer due to the presence of oxide defects present on the surface.

Compared to the traditional processes, AlSi10Mg alloys made by SLM and anodized have greater properties if the process is specifically controlled.

INDEX

UNIVERSITÀ DEGLI STUDI DI PADOVA	1
SUMMARY	9
INTRODUCTION.....	23
1. LITERATURE REVIEW	27
1.1. ADDITIVE SELECTIVE MELTING.....	27
1.1.1. <i>Additive manufacturing</i>	27
1.1.2. <i>Influence of alloying elements in AlSi10Mg alloys</i>	31
1.1.3. <i>Structures of AlSi-alloys in the SLM process</i>	36
1.2. ANODIZING.....	42
1.2.1. <i>Natural anodizing and how it works</i>	44
1.2.2. <i>Materials that can be anodized</i>	46
1.2.3. <i>Parameters</i>	47
1.2.4. <i>Ancillary treatments prior to anodizing</i>	52
2. EXPERIMENTAL PROCEDURE.....	57
2.1. INTRODUCTION	57
2.2. ANODIZING.....	57
2.2.1. <i>Anodizing preparation</i>	63
2.3. HARDNESS.....	66
2.4. WEAR TEST.....	68
2.5. CORROSION AND EIS.....	70
3. RESULTS.....	77
3.1. CHEMICAL COMPOSITION	77
3.2. QUALITATIVE AND QUANTITATIVE ANALYSIS	77
3.2.1. <i>Macrostructure analysis</i>	78
3.2.2. <i>Microstructure analysis</i>	82
4. ANODIZED SAMPLES RESULTS.....	91
4.1. ANODIZATION	91
4.2. HARDNESS AND WEAR TEST.....	101
4.3. CORROSION TESTS.....	106
5. CONCLUSIONS	115
ACKNOWLEDGEMENTS	119
BIBLIOGRAPHY	121
APPENDIX	127

Index of figures

Figure 1.1: 3D printing material scheme	28
Figure 1.2: Schematic representation of the SLM process[7].....	29
Figure 1.3: Schematic illustration of the internal laser drying process.....	30
Figure 1.4: Fluidity of AlSi-alloy vs % Si in the alloy	33
Figure 1.5: Phase diagrams of AlSi in different fields of applications	34
Figure 1.6: Laser scanning strategies reported in the literature	36
Figure 1.7: Macrostructure of the SLM AlSi9Cu3Fe alloy in (a) transversal and (b) longitudinal section.....	37
Figure 1.8: Comparison between (a) as-cast (HPDC) and (b) SLM microstructures	38
Figure 1.9: Fine cellular substructure AlSi9Cu3Fe in (a) transversal and (b) longitudinal section.....	39
Figure 1.10: MPBs on the surface perpendicular to the building platform of AlSi10Mg.....	40
Figure 1.11: SEM image of AM surface near a melt pool border.....	41
Figure 1.12: Scheme of microstructure divided into zones thanks to SLM[22]	42
Figure 1.13: Anodizing scheme of setup[23].....	43
Figure 1.14: Typical structure of an Al Anodized[24].....	43
Figure 1.15: Lateral vision of an anodized Al sample	44
Figure 1.16: Vision from the top of an anodized Al sample.....	44
Figure 1.17: Anodizing mechanism.....	45
Figure 1.18: Behaviour of Si particle during anodizing [28].....	49
Figure 1.19: Colour changing of Ti6Al4Va because of DC voltage (in V).....	50
Figure 2.1: Sample arrived from Pretoria (100x40 mm) on the bottom. Sample cut in Jönköping University (20x20 mm) on top	58
Figure 2.2: Planes defined with Miller's index.....	59
Figure 2.3: Sample mounted in a no-conductive resin	62
Figure 2.4: Sample mounted in a conductive resin	62
Figure 2.5: Sample during the anodizing process.....	63
Figure 2.6: Oven for porous sealing.....	64
Figure 2.7: Eddy current method scheme on Fischer Isoscope	65

Figure 2.8: Cross section of samples Ya4 and Za4 polished, into resin	66
Figure 2.9: Characterization of Berkovich tip.....	67
Figure 2.10: Ball-on-disc configuration friction test (a), (b) +CSM apparatus (c) .	68
Figure 2.11: profile after wear test.....	70
Figure 2.12: EIS setup.....	72
Figure 2.13: Circuit in porous section R(RC)(RC)	73
Figure 2.14: Equivalent circuit R(C(R(CR))).....	74
Figure 2.15: Example of Bode diagram obtained after EIS measurements in 9 cycles in 24 hours.....	75
Figure 3.1: Micrography of XY1 sample.....	78
Figure 3.2: Micrography XZ1 sample.....	79
Figure 3.3: XZ1 after Keller' etching – overlapping detail (in green).....	80
Figure 3.4: YZ1 sample	81
Figure 3.5: a) Melting pool borders and b) HAZ of XZ1	82
Figure 3.6: Surface parallel to the growth direction (XZ1) a) after EDS mapping: Si in purple matrix b). c) and d) reveal a uniform distribution of Al and Mg	83
Figure 3.7: Surface perpendicular to the growth direction (XY1) a) and after EDS: Si in purple network b) c) and d) reveal a uniform distribution of Al and Mg.....	84
Figure 3.8: Optical image of a region in the surface of the cast alloy AlSi10Mg [35]	85
Figure 3.9: Optical image of the surface parallel (XY) to the building platform of SLM AlSi10Mg	86
Figure 3.10: AlSi10Mg in XY plane a) cast b) in AM-SLM at the same magnification. In white, the Si phase [35]	87
Figure 4.1: Time - Current density.....	92
Figure 4.2: Thickness [μm] of the anodized coating measured with Eddy current method	93
Figure 4.3: Cross section of samples Ya4 and Za4 polished into resin	95
.....	95
Figure 4.4: Cross section of (X)Ya4 after anodizing and some values of oxide thickness.....	95
.....	96

Figure 4.5: Cross section of (X)Za4 after anodizing and some values of oxide thickness.....	96
Figure 4.6: Thickness [μm] of anodized coating with cross-section method.....	96
Figure 4.7: AlSi10Mg made by casting cross section, after 20 min of anodizing[35]	97
Figure 4.8: Base material (in blue), the oxide layer on lateral. EDS mapping of a cross section of perpendicular section.	98
Figure 4.9: EDS mapping highlighting the presence of O, Al, Si and Fe in the oxide layer of Ya4 sample	99
Figure 4.10: EDS mapping, cross section of perpendicular surface (Ya4 sample), highlight a crack.....	99
Figure 4.11: EDXS on a cross-section closer to the presence of a crack.....	100
Figure 4.12: Berkovick imprints on oxide layer (Ya42)	101
Figure 4.13: Berkovick imprints on oxide layer (Za41)	101
Figure 4.14: Berkovick results in y41-y42 and z41 and z42.....	102
Figure 4.15: Hardness in GPa of a) SLM anodized b) SLM c) cast AlSi10Mg....	102
Figure 4.16: BSED wear track with adhesion phenomena and some lateral surface cracks	103
Figure 4.17: Lateral cracks due the wear test, close to the spin ball track.....	104
Figure 4.18: Glimpsed substrate after wear test.....	105
Figure 4.19: Magnitude and phase of a) Ya and b) Za; in blue the phase; in green-yellow, the modulus	107
Figure 4.20: Evolution of the Rp of Ya and Za samples during the immersion time	108
Figure 4.21: SEM of a parallel direction after EIS	109
Figure 4.22: Detail of Ya1 a) and EDS of it b) c).....	109
Figure 4.23: EDXAS mapping of the pitting corrosion on the Ya2 sample	110
Figure 4.24: Perpendicular side (Za1) after EIS	110
Figure 4.25: Detail of Za1 after EIS a) and the element composition b)	111
Figure 4.26: Cross section after anodization and corrosion attack	112

Index of formula

Formula 1.1 Anode reaction	44
Formula 1.2 Cathode reaction	44
Formula 1.3 Overall reaction	45
Formula 2.1 Wear rate formula	69
Formula 2.2 Volume formula	69
Formula 2.3 Sliding distance	69
Formula 2.4 Wear rate simplified formula.....	70
Formula 2.5 Metal dissolution	71
Formula 2.6 Reduction of H.....	71
Formula 2.7 Reduction of O in acid and basic environment.....	71
Formula 2.8 Reduction of metallic ions	71

Index of tables

Table 1.1: Common anodized materials	47
Table 1.2: Thickness of layer and usage.....	48
Table 1.3: Parameters of traditional and hard anodizing	51
Table 2.1: Chemical samples composition conducted with spectroscopy	57
Table 2.2: Renamed samples no anodized.....	59
Table 2.3: Grinding and polishing steps.....	60
Table 3.1: Chemical composition conducted with spectroscopy (%wt.)	77
Table 3.2: Renamed samples no anodized.....	78
Table 3.4: Scale areas of Al pool in laterals (XZ1 and YZ1)	81
Table 4.1: Renamed anodized samples	91
Table 4.2: Oxide growth rate during anodizing of specimens (in H ₂ SO ₄ electrolyte) in $\mu\text{m}/\text{min}$ [12]	94
Table 4.3: Corrosion time cycle.....	106

Introduction

In recent years, lightweight design has become a significant focus for industries ranging from automotive to aerospace. Lightweight materials and components can reduce carbon dioxide emissions, save energy, and reduce costs.

Additive manufacturing, or 3D printing, is one such technology that has great potential to address these issues due to the considerable flexibility in terms of shapes (geometry and dimension) and materials. Nowadays is viable to print not just polymers but also metals and create combinations of different materials. [1]

Selective laser melting (SLM) is one of the additive manufacturing methods that can satisfy different requirements in terms of complexity thanks to computer model design (CAD) that can offer a high degree of freedom in terms also of the requested shape and then, according to the file created by CAD, the SLM process create a layer-by-layer component. The as-built parts created are so well done (for instance, in terms of surface roughness) that can be ready for use. Microstructure and evolution of solidification have been studied recently, finding correlations between parameters such as laser power and scan speed (for instance, increasing those two is possible to observe an increase of density). [2]

One of the ideas is to combine one of the most used Al-alloy with this new production system and study how the process response is usually made for increasing mechanical properties in standard production.

The Al-Si alloys have outstanding high thermal conductivity, fluidity, low thermal expansion coefficient and excellent castability. All those properties made AlSi10Mg the right candidate for casting and shaping in SLM processing.

The object of this thesis is to understand the impact of anodizing process in AlSi10Mg made by selective laser melting. The result will highlight the potential of additive manufacturing and of the anodizing process.

A different macrostructure is observed for AlSi10Mg during SLM compared to the casted version. This will be due, in particular, thanks to the rapid solidification. Selective laser melting process increased the microstructure homogeneity but also generated much more porosity (by the way, topology and size of the pores can be controlled using various processing parameters [3])

During anodizing, there is a generation of the porous structure of the oxide on the cleaned bulk. The oxide layer has a hexagonal structure, with a pore in the middle; maxing a cross-section is possible to see the dimension of the porous layer till it reaches the base material. This study highlighted the hardness of this oxide and compared it with components not anodized and made with SLM and with casting operations.

Another study was done thinking about typical environments in which those components can be used. Recreation of an outdoor situation is done by immersing components in a saline solution at 3% and studying the degradation of the oxide layer created during anodizing.

1. Literature review

1.1. Additive selective melting

1.1.1. Additive manufacturing

Additive manufacturing (AM) is a technique regulated by the ISO/ASTM 52900, based on “*geometrical representation, create a physical object by successive addition of material, layer by layer*”[4].

Additive manufacturing, rapid prototyping (RP), rapid manufacturing (RM) or additive layer manufacturing (ALM) are all technologies that share this approach [3], [5]:

1. The creation of a 3D object is designed using computer-aided design (CAD) software.
2. Convert the file in STL format (With a file preparation software interface) used by the 3D printing/additive manufacturing machine.
3. Break the 3D STL geometry into individual slices of constant thickness, creating a 2D representation of the object. The computer numerical control program (CNC) uses these layers as a blueprint.

Thus, the manufacturing process is performed by a machine controlled by a CN, which creates layer by layer the desired object.

Various materials require different systems for fusing the layers together.

The following scheme (**Figure 1.1**) is a possible classification of the different processes of AM (divided by material) discovered until now [6]:

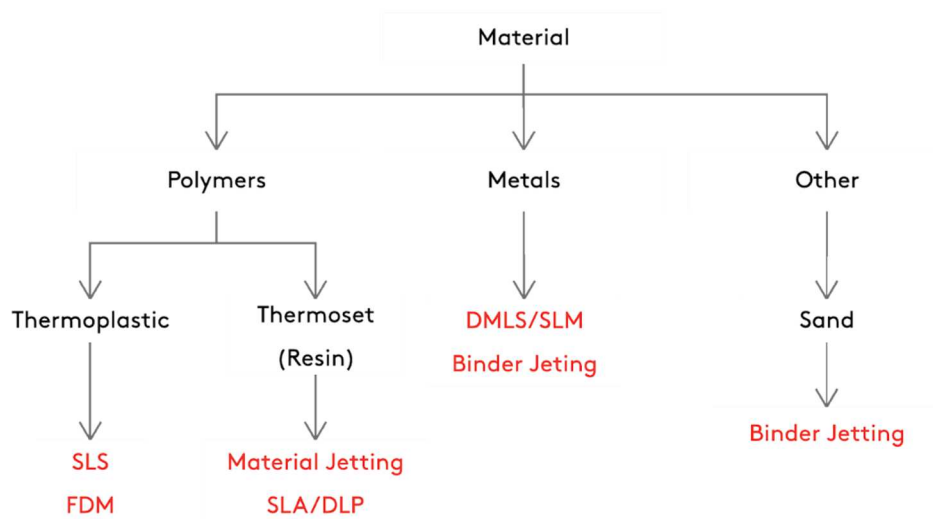


Figure 1.1: 3D printing material scheme

Selective laser melting (SLM) is a technique of AM based on the deposition of a thin layer of powders on a building platform. The powder metal layer is entirely and keenly melted by a focused laser beam. At this point, the building platform is lowered, and a new powder melt layer can be settled. The process will be repeated layer-by-layer until the figure is done (**Figure 1.2**):

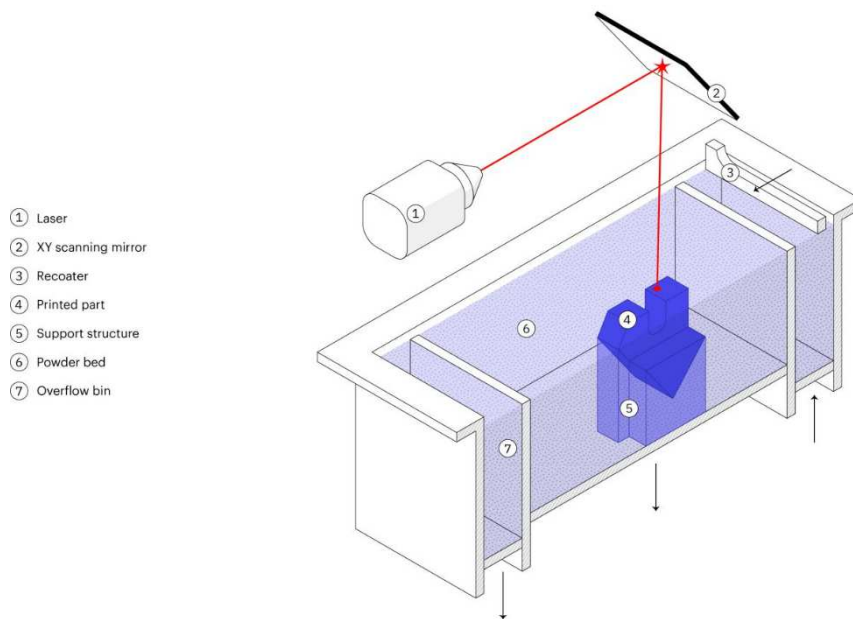


Figure 1.2: Schematic representation of the SLM process[7]

In order to don't degrade the quality and the mechanical properties of the product, the process takes place in an inert chamber full of argon. The particle size of the powder is smaller than $60\ \mu\text{m}$, and it is consolidated by using a high-energy density fibre laser. The powder is deposited on a mobile build plate, which moves along the z -axis, and it has a thin layer thickness between 25 and $50\ \mu\text{m}$. After the powder distribution on the build plate, the laser beam scans the powder bed and melts the new layer (**Figure 1.3**) on the x - y plane with the previous layer, and after the build plate lowering, the process restarts.

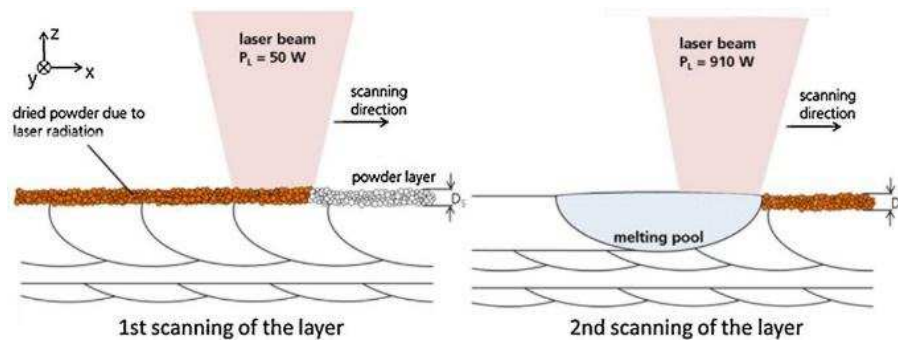


Figure 1.3: Schematic illustration of the internal laser drying process

Use of AM

Parts manufactured by SLM can have an internal and external complex shape, no easier to make with other methods. Because of costs higher than processes for optimized parts for high-value engineering applications.

Thanks to the high flexibility of the process to generate parts of different sizes and complex geometry, the fields of application are different:

- Automotive
- Consumer
- Medical
- Aeronautical
- Power and communication
- Manufacture and production

Compared to the traditional subtractive manufacturing techniques (like milling, cutting and drilling), AM allows a reduction of wasted material, tooling and fixture (presence of already consolidated assembled parts and also a reduction of parts in terms of numbers), weight (based on design loads) and products lead time [8].

But AM also has some disadvantages related to the accuracy of surfaces (can result in stair stepping, porosities, hot cracking, anisotropy [9]),

process speed (time-consuming), size of components, skill shortages, software (need an expert in CAD) and expense (may be prohibitive).

1.1.2. Influence of alloying elements in AlSi10Mg alloys

The fields of application of AM also require a material that can fit with the described process. The perfect candidate nowadays is aluminium.

This is also because of different properties like low weight (after steel and copper), high corrosion resistance, non-toxicity, high corrosion resistance, high thermal and electrical conductivity, high weldability, low power radiation and good formability.

Aluminium can be pure, can come from scraps (primary and secondary fusion) or can be made as an alloy (called *light alloy*).

Al-alloys are made in order to improve aluminium properties by adding elements; the main ones are:

- Silicon improves the fluidity of the alloy, decreases shrinkage porosity (so it improves castability and feeding capacity), and reduces the expansion coefficient. It can also increase mechanical properties (UTS, YS, etc.) as a hard phase. Si also decreases the density, thermal conductivity and ductility of Al alloys. Increase brittleness and reduce hot tearing.
- Magnesium increases hardness, strength, corrosion resistance, polishing, anodizing, and painting. Decrease castability.
- Manganese decreases ductility but increases mechanical properties
- Copper increases the mechanical resistance, especially the hot mechanical properties. Improve machinability but decrease castability and corrosion resistance.

- Zinc combined with magnesium gives higher mechanical resistance, but because of interactions with other elements, it decreases the corrosion resistance
- Iron in casting reduces die solidification phenomena and ductility, increasing die life and die life

Chemical compositions of Al-alloys are regulated by international standards such as EN 1706:2010 European Standard, CIS for Russia, JIS for Japan, A.A. for the US, BS for UK and ETIAL for Turkey. Each composition has an exact range of % for each element.

Those are the main common elements in Al alloys. Depending on the concentration of Si is possible to identify three categories of Al-Si alloys: hypoeutectic, eutectic and hypereutectic alloys. Where the eutectic point is at 12.6-13% of Si in weight (close to this percentage, there is also the maximum fluidity, as mentioned before, and quite visible in **Figure 1.4**[10]).

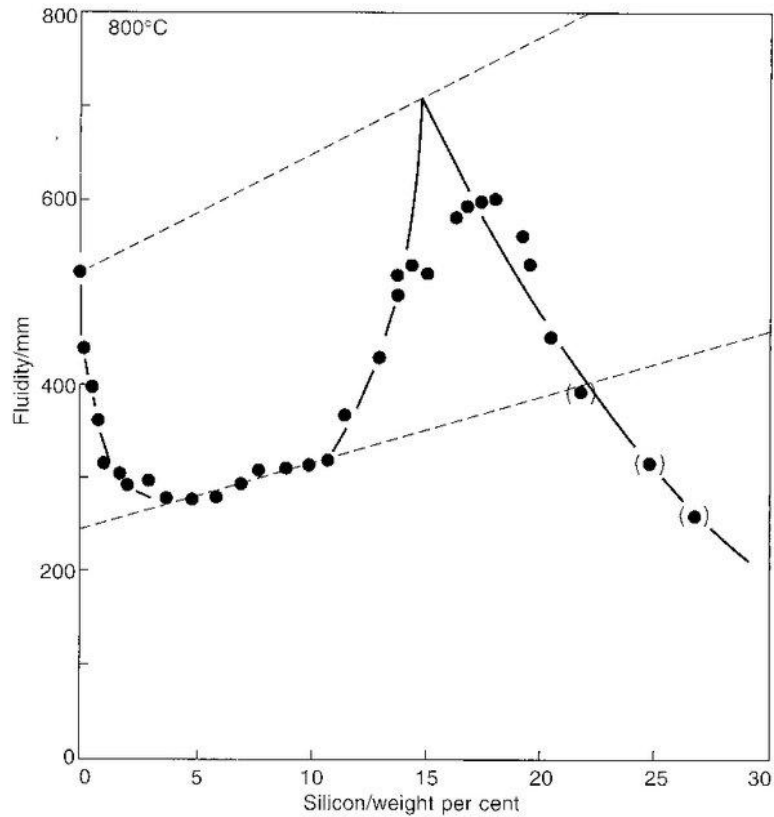


Figure 1.4: Fluidity of AlSi-alloy vs % Si in the alloy

It is possible to increase the properties of Al-Si alloys by adding other elements based on what are the final product requests (**Figure 1.5** shows an example of properties). As anticipated, the common ones are copper and magnesium.

The addition of copper in the Al matrix increase strength and ductility. In Al-Si alloys aims to increase hardness and creep resistance. However, Cu reduces corrosion resistance, so in this case, adding magnesium is a valid alternative.

The addition of magnesium, as the Cu, thanks to Mg_2Si (in the presence of Cu is $AlCu_2Mg$) particles in Al-matrix increases strength and hardness in heat treatments. On the other side, having more than 0.7%Mg decrease the ductility.

Studies also give a lot of other elements that can be added in a small amount (so small that they are not present in the name of the alloys) in order to change properties, morphology (e.g. Sr, Ti, Cr, Be), etc. of the Al-alloys.[11]

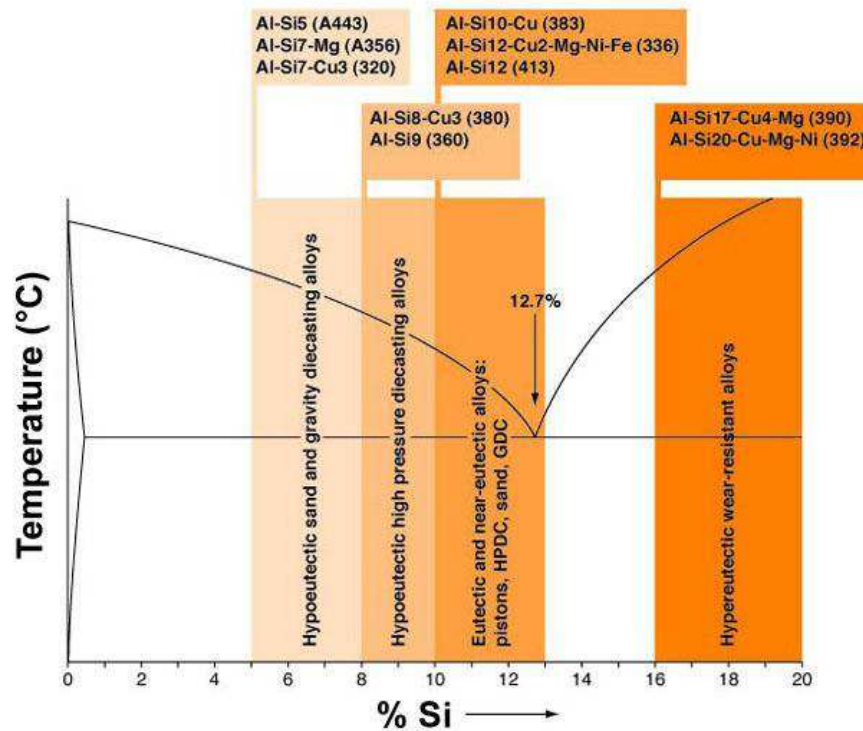


Figure 1.5: Phase diagrams of AlSi in different fields of applications

Among various aluminium alloys, cast AlSi10Mg alloy is the most employed aluminium alloy for additive manufacturing [12] because of good corrosion resistance, high specific strength and excellent processability.[13]

It is the wide alloy used in the industry thanks to due the short solidification range (557°C-597°C): this hypoeutectic composition is

close to the eutectic point (12.6% Si), visible also in the phase diagram (Figure. 1.5[14]).

The combination of Si and magnesium in a small amount (0.3-0.5%) cause the formation of Mg_2Si precipitates when the alloy is exposed to a natural or artificial ageing treatment. These precipitates will then cause hardening of the alloy, thus improving the strength properties of the alloy. [15], [16]

In general, Al-Si alloys can be manufactured by almost all casting processes, such as high and low-pressure die casting, gravity die casting and also SLM [15].

1.1.3. Structures of AlSi-alloys in the SLM process

The morphology of AM specimens is unique and depends on how the scanning laser works.

Usually, every layer done by the SLM process was divided into square boxes representing a chessboard (Strategy 1 and 4 in **Figure 1.6**) in order to create a ‘chessboard’. The scanning direction (laser tracks) changed with each layer by 90° , so it is possible for types of elongated zones to overlap perpendicularly; this happens in the building direction[17], [18]

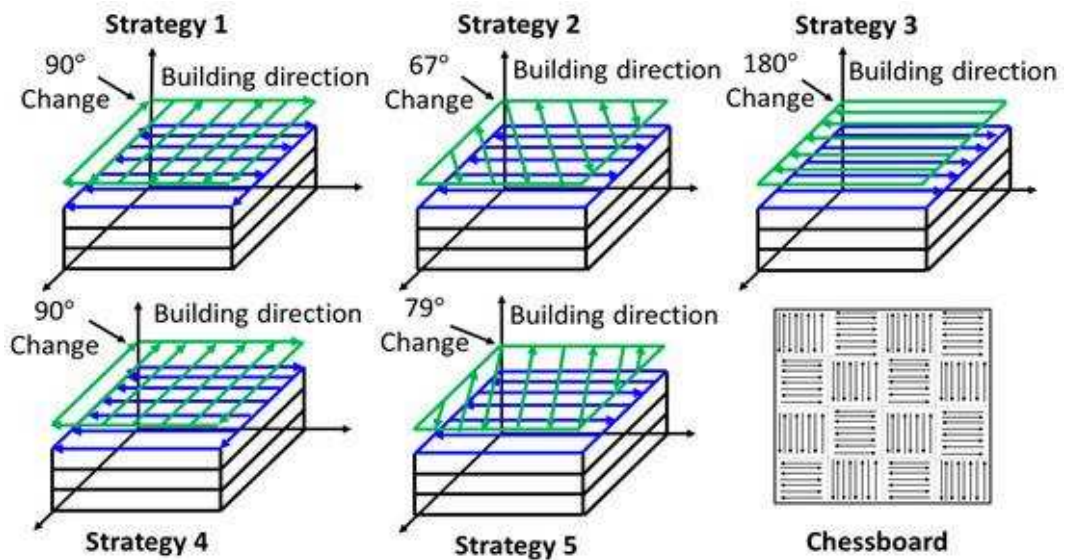


Figure 1.6: Laser scanning strategies reported in the literature

As numerous works show, this strategy is pretty easy to recognize also with the just aim of a LOM microscope (**Figure. 1.7 a**) and **b**))[17]

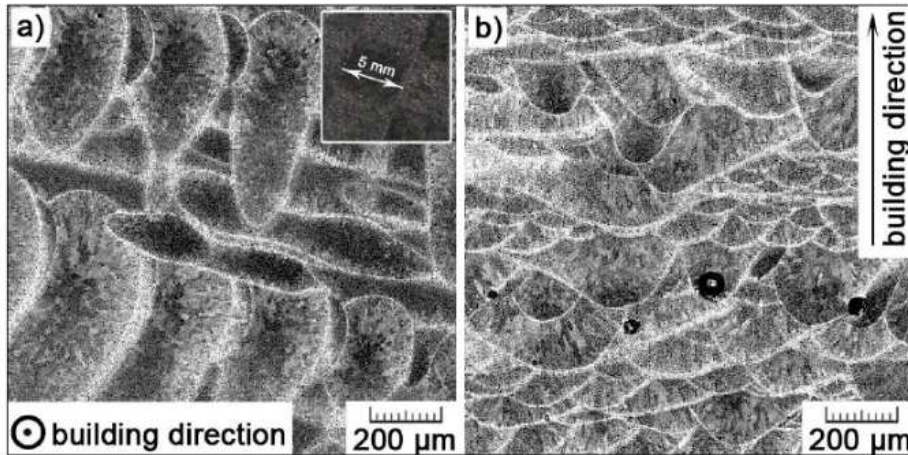


Figure 1.7: Macrostructure of the SLM AlSi9Cu3Fe alloy in (a) transversal and (b) longitudinal section

Due to the laser beam, melt pools were formed transiently. The solidification makes this pool visible immediately. The optical image in AM samples shows that the melt pools and the melt pool borders (MPBs) are visible because the microstructure is coarser at the borders of the melt pool.

This working thesis was done with samples of AlSi10Mg alloy, hypoeutectic. It is characterized by a structure composed of α -Al grains and surrounded by α -Al/Si eutectic microstructure.

According to the phase diagram, the microstructure is characterized by the size and arrangement of the following:

- Eutectic Si-particles (light phase)
- Supersaturated matrix of α -Al (dark phase)

In casting, the microstructure of Al-Si alloys presents an α -Al matrix and an Al-Si eutectic structure. As said before, the amount of eutectic structure depends on the Si level in Al-Si alloys. What most influences

the microstructure of an Al alloy is the cooling rate. An increase in cooling rate leads to a finer microstructure of the eutectic phase with small secondary dendrite arm spacing (SDAS) and a small size of intermetallic, while a low cooling rate results in a coarse microstructure with big and flake-like Si particles. [19]

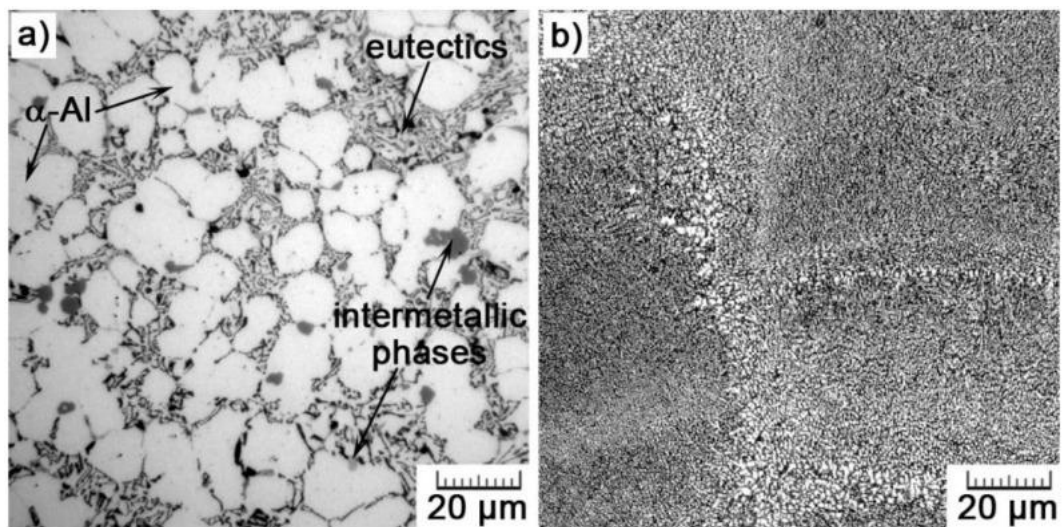


Figure 1.8: Comparison between (a) as-cast (HPDC) and (b) SLM microstructures

In SLM, due to the higher cooling rate, it is impossible that can happen the formation of dendrites with multiple arms. Therefore, very fine cells are formed. They elongate in the longitudinal direction of (with the highest temperature gradient) (**Figure 1.9 a) b)**).

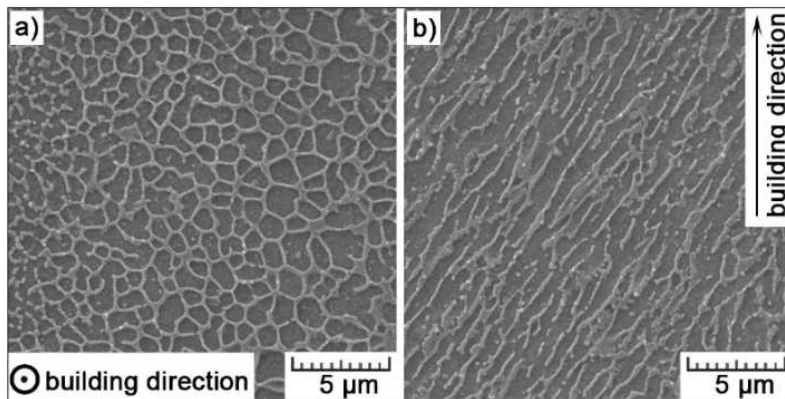


Figure 1.9: Fine cellular substructure AlSi9Cu3Fe in (a) transversal and (b) longitudinal section.

The fine dispersion of fibrous Si networks in the Al matrix has a positive effect on the mechanical properties of the SLM specimens. [20] The figure above shows the 3D network that encloses the α -Al. These cells have an elongated shape in the longitudinal section (**Figure 1.9**) with an average length of 0.4 to 1 μm . In the transversal section, the shape is more circular, with an average diameter ranging from 0.3 to 0.6 μm (**Figure 1.10**).

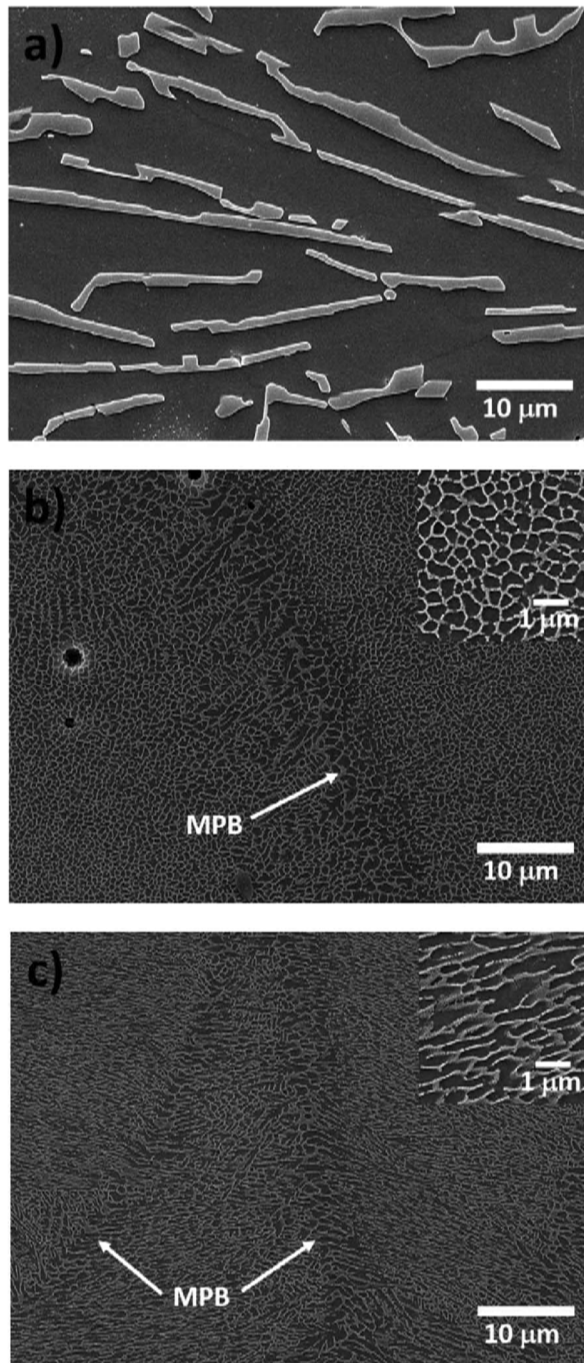


Figure 1.10: MPBs on the surface perpendicular to the building platform of AlSi10Mg

The transition of the laser beam affects the material by the heat, and it creates, between the MPB, a zone called *heat-affected zone* (HAZ). In the HAZ, the intercellular network has coarsened into idiomorphic silicon particles.

Here the intercellular network is broken up into idiomorphic particles due to an increase in the diffusion rate of silicon (**Figure 1.11**) [21]

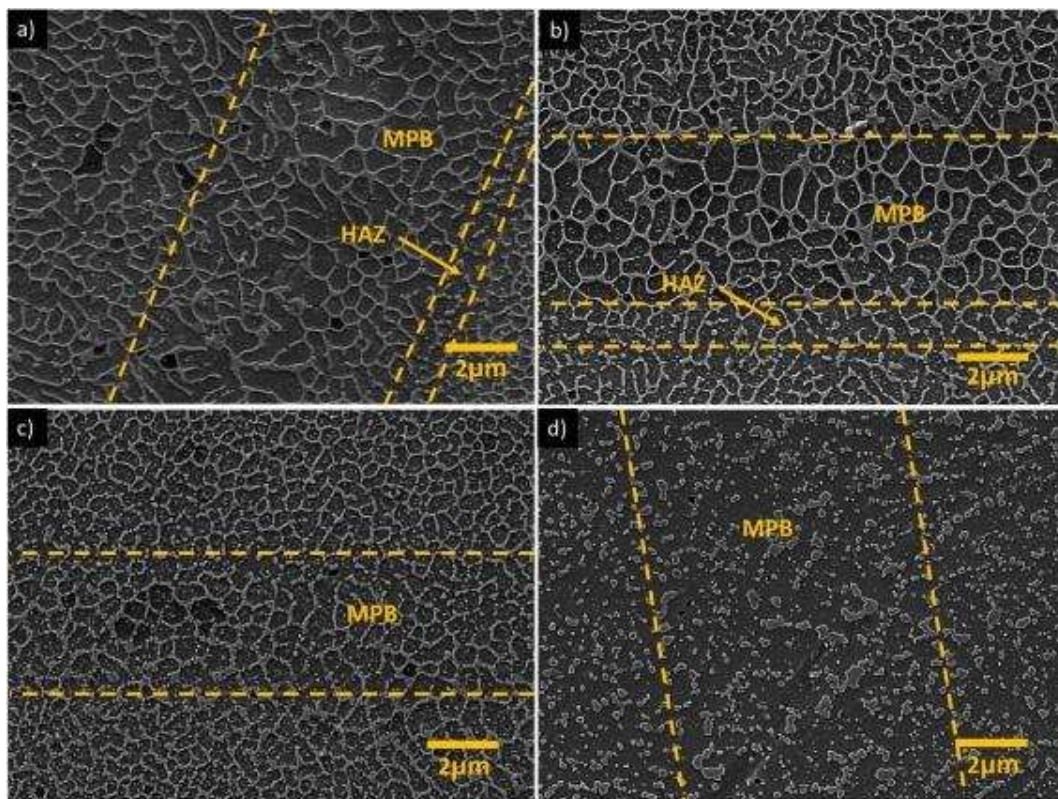


Figure 1.11: SEM image of AM surface near a melt pool border

A clear and schematic diagram (**Figure 1.12**) of the formation of the three-zone in the SLM process of an AlSi10Mg alloy is given by the work of Xhie Liu [22]. T_s has identified the solidus temperature, and T_l identifies the liquidus one.

- Fine zone ($T > T_L$): it is where is located the melt pool, and from the centre to the hedge of this zone, the microstructure is gradually refined.
- Coarse zone ($T_s < T < T_L$): it is at the border of the melt pool; the length of α -Al is much smaller than that refine zones but wider/broader.
- Heat effect zone (HAZ) ($T < T_s$): in this area, the Si network is broken into small particles (because here metal is not melted by laser beam, but the laser creates a kind of heat treatment, so Si precipitates from the supersaturated Al, became Si particles that form and growth. In the end, the cells' boundary disappears).

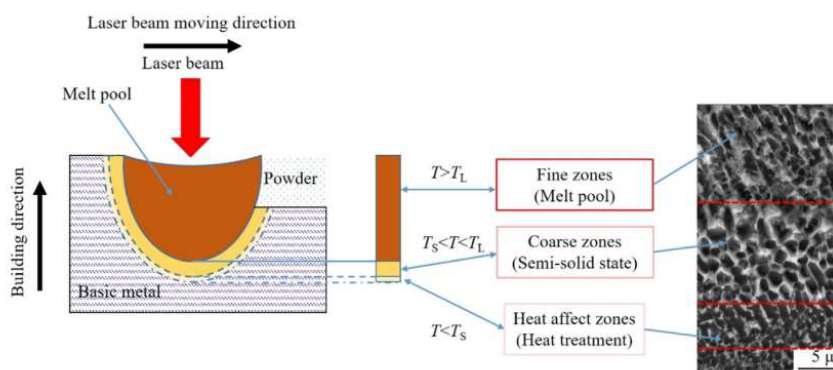


Figure 1.12: Scheme of microstructure divided into zones thanks to SLM[22]

1.2. Anodizing

Anodizing is a surface conversion process where the base material is converted into an oxide (e.g. Al_2O_3) during an electrolytic process. Anodizing can be carried out in many different chemical solutions depending on the intended application.

The system is composed of these parts (**Figure 1.13**):

- 1) Anode (the material we want to anodize, e.g. Al)

- 2) Cathode: Pt/Ti plate
- 3) Ions flow (+ from anode to cathode and – from cathode to anode)
- 4) Bath (e.g. sulphuric acid), the electrolyte

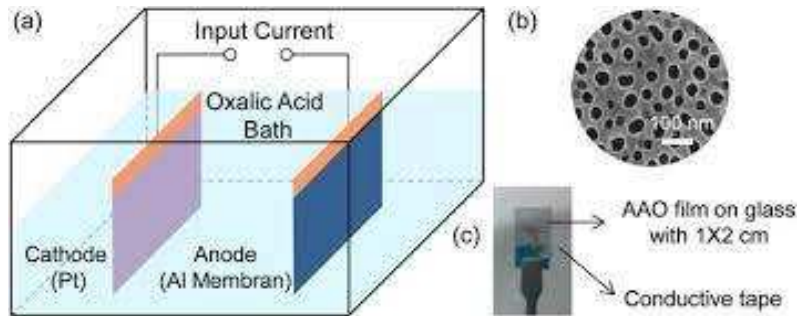


Figure 1.13: Anodizing scheme of setup[23]

Applying a current (or an anodic potential), the oxide layer starts to grow.

Due to the current, ions migrate on the anode, that thanks to its characteristics, accepts O and creates a first oxide layer called a *barrier layer* and a second one, much more porous on the surface (**Figure 1.14**)

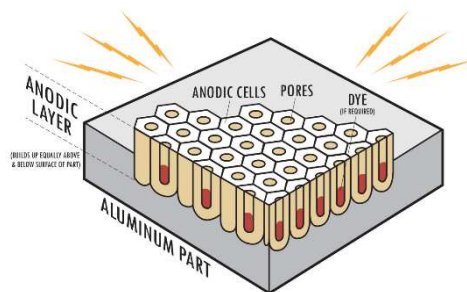


Figure 1.14: Typical structure of an Al Anodized[24]

The porous layer can be used for further processing like painting (e.g. in order to avoid flaking).

So an anodizing treatment is easily recognizable in lateral and top vision (**Figure 1.15** and **1.16**[25]). The structure of aluminium oxide is very peculiar: ordered tubes grow perpendicular to the surface. Tube size is very homogeneous and depends on the process parameters.

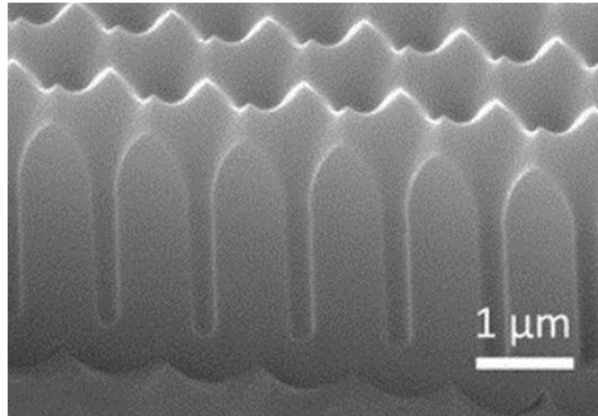


Figure 1.15: Lateral vision of an anodized Al sample

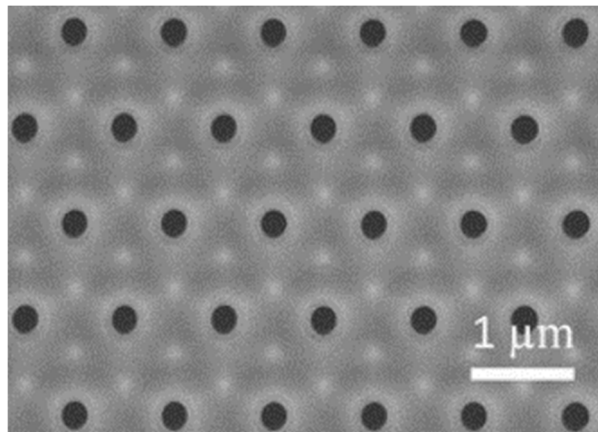
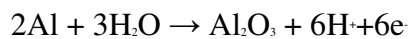


Figure 1.16: Vision from the top of an anodized Al sample

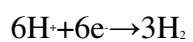
1.2.1. Natural anodizing and how it works

The anode reaction takes place on the anode surface to produce anodic oxide:



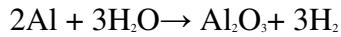
*Formula 1.1
Anode reaction*

There is a reduction process taking place on the cathode surface:



Formula 1.2 Cathode reaction

The overall reaction:



Formula 1.3 Overall reaction

Applying a constant anodic potential current varies with time because of the mechanism changes in the oxide growth.

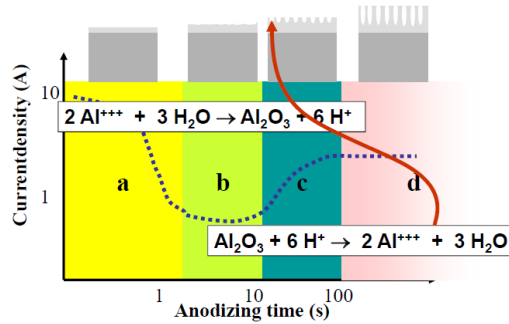


Figure 1.17: Anodizing mechanism

The oxide layer growth takes place in several steps (**Figure 1.17**):

Step a) in **Figure 1.17** shows the uniform oxidation and formation of the first oxide layer. The current in this step will be relatively high since current only passes through the metallic aluminium or its alloys. When full coverage of the oxide layer has been reached, the current will decrease approximately linearly as the thickness of the oxide layer increases since the oxide layer (alumina Al_2O_3) is a good insulator. A compact oxide film starts to grow, and the current tends to decrease because the surface becomes more and more resistive

The increase in thickness results in a decrease in the current taking place in step b. At the end of *step b*), the tendency of the curve turns upwards because of small imperfections in the oxide layer. These small imperfections are formed by the concentration of the current or electrical field in areas with thinner oxide than on the rest of the surface, thereby increasing both the formation as well as dissolution of the oxide layer. At this point, the dissolution of the oxides starts parallelly to further Al oxidation, and this induces the formation of pores at step c.

Step c) the oxide is some microns thick, a localized dissolution process starts, and oxidation continues with a tubular structure: at this point current increases again.

The structure of nano/micropores is regular and has a hexagonal structure. From the cross-section view, the oxide layer consists of two layers, named the porous layer and the barrier layer (**Figure 1.17**). Since the dissolution reaction is started, the oxide thickness inside the pore is reduced, and the current will flow to repair the damage.

Step d) the current reaches a constant level where the rates of dissolution and formation of the oxide layer reach a steady state.

1.2.2. Materials that can be anodized

Anodizing process is, in general, used in order to increase wear resistance, generate corrosion protection and also give some aesthetic appeal (multicolour, matt or shiny finishing).

Metals, in order to be anodized, need to maintain a stable oxide layer. Just watching the commercial trend, it is pretty understandable who can be the candidate anodes (Table 1.1):

<i>Material</i>	<i>Decoration</i>	<i>Protection Resistance</i>	<i>Examples</i>
Stainless steel	X		Jewellery
Titanium	X		Dental implants
Niobium	X		Numismatics
Zinc	X	X	For lab and research purposes

Magnesium		X	Car parts
Hafnium		X	Apollo Lunar Lander Modules engines
Aluminium	X	X	Apple' products, carabiners, etc

Table 1.1: Common anodized materials

As said before, Al-alloys are widely used in different fields, and a process of anodizing improves corrosion protection and surface hardness.

Two types of aluminium anodizing are available commercially:

1. Traditional anodizing: good corrosion protection (that can be further improved by sealing the porous structure) and the possibility to add colours into the layer (Type II). The candidate's alloys for this process are 1xxx, 5xxx and 6xxx (ASTM std).
2. Hard anodizing: with excellent corrosion resistance and good surface mechanical properties such as higher hardness and wear resistance. (Type III). For alloys with low Cu and Si content [26]

1.2.3. Parameters

Parameters that can influence the process are different: type of electrolyte, voltage, bath temperature and material.

It is possible to obtain different thicknesses and regulate them related to the application field (**Table 1.2** [27]).

<i>Thickness [μm]</i>	<i>Usage</i>
5	For decoration, jewellery, arts and craftworks. Only suitable for surfaces used indoors.
10	Indoor or clean outdoor environment (e.g. reflectors, fitting, decorative plates and sports equipment).
15	Outdoors or metals. Surfaces exposed to medium indoor wear.
25	Heavy or normal outdoor applications (e.g. ships). Indoor surfaces exposed to the chemical or moist-containing atmosphere in connection with production plants, process lines and equipment used in (e.g. food industry).
25-250	The extensive form of corrosion or wear. Especially outdoor applications in highly corrosive environments (e.g. mounts, engines and wheels).

Table 1.2: Thickness of layer and usage.

The thickness layer of Type II is usually below 25 μm . The structure is well-oriented in hexagonal cells and grows homogeneously and perpendicular to the surface. If the material meets a particle of the alloy, it can react by decreasing the oxidation and enveloping it.

In the case of AlSi alloys, the Si reacts to form the Si-O at a much slower rate of the Al oxidation. Then the Si particle is embedded in the oxide layer, and the Al phase below the Si particle remains not anodized. This event is easy to recognize because the volume expansion around the Si

particle can create localised stress visible as cracks and voids. [28]

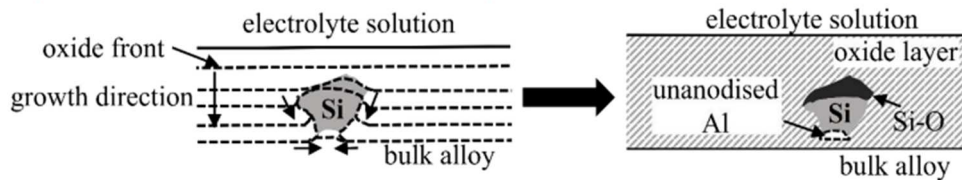


Figure 1.18: Behaviour of Si particle during anodizing [28]

Above 25 μm of thickness, there is the Type III anodization.

Bath composition

Different electrolytes allow the classification of anodizing processes:

- Sulfuric acid anodizing
- Chromic acid anodizing
- Other chromium-free anodizing processes

The commonly used one is the sulfuric electrolyte: depending on voltage and current is possible to obtain decorative/protective and hard anodizing (parameters examples will give in the next paragraph). The chromic bath is used in the aeronautic field because it allows to have a better response to corrosion attacks and also gives an adhesion to painting. However, chromium is toxic, so it is substituted with a phosphoric bath (which also allows a deep bonding).

Voltage and current density

Increasing voltage (and current density) can also increase oxide thickness and influence colour.

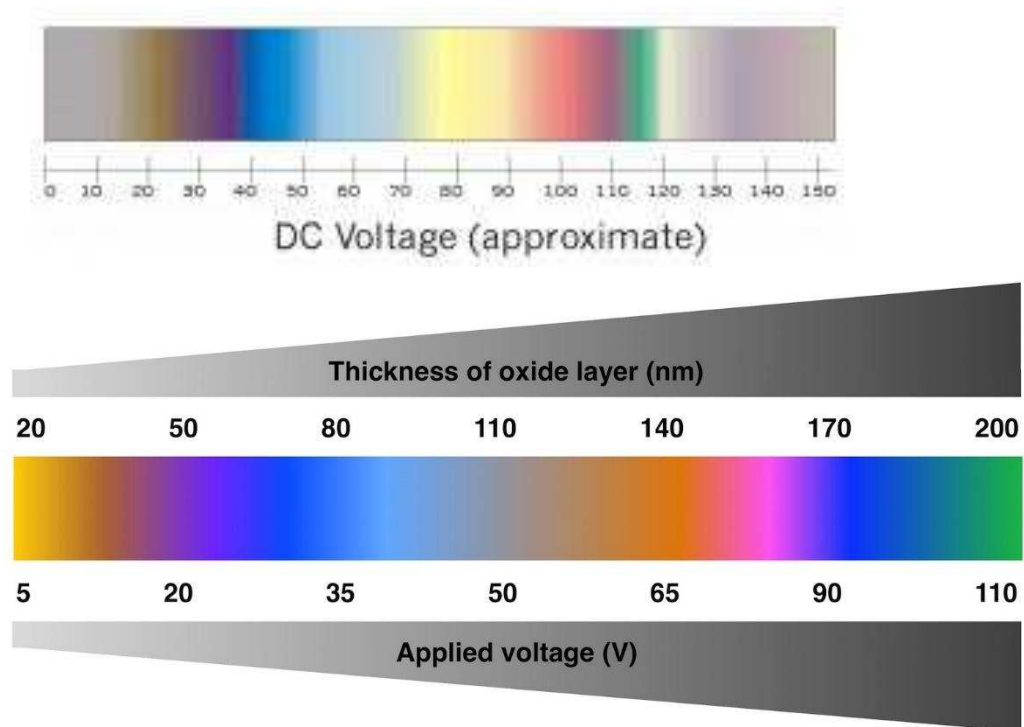


Figure 1.19: Colour changing of Ti6Al4Va because of DC voltage (in V)

Approximately for a Ti6Al4Va, the pink region in **Figure 1.19** [29] corresponds to an oxide layer of 160 nm. For a Type II process is between 1 and 1.5 A/dm².

Electrolyte temperature

Must be controlled: for Al, higher temperatures can break the barrier layer. But a moderate one allows the growth of pores, and so, for example, can absorb better colour pigments.

Increasing temperature increase thickness and, as said before; also an increase of current density can increase thickness; combining both parameters is possible, in general, to increase also the thickness to 1.4 μm/V.

It is crucial to maintain the same temperature during the process in order to not damage the oxide layer and create cracks.

Because of electrical resistance heating, the bath temperature tends to increase during the anodizing process. So some ice cubes are used to maintain the bath.

Alloys

Different materials can give different colours, brightness and properties because of different oxides formed.

Changing parameters allows the control of the anodizing process, for instance, of the aluminium. This means that literature gives some ‘recipes’ to follow (**Table 1.3** [30])

<i>Parameters</i>	<i>Traditional anodizing</i>	<i>Hard anodizing</i>
Bath concentration g/l [H ₂ SO ₄]	180-200	100
Current density A/dm ²	1.2-2	2-5
Voltage V	18-22	15-120
Temperature °C	5-10 must be <21°C	0-15
	15-25 must be <20°C	
Time min	10-60	

Table 1.3: Parameters of traditional and hard anodizing

The industrial setup for AlSi is 129 A/m², 35V, 20°C per 10-60 min.

At the end of the process, the hard anodizing has an oxide that is more compact, thicker and hard than a traditional one.

1.2.4. Ancillary treatments prior to anodizing

There are some steps that ensure an excellent anodizing process [31]

1. *Cleaning*: the surface must be cleaned in order to remove grease and dirt.
2. *Pre-Treatment*:
 - Etching: minor surface imperfections are removed with hot solutions of sodium hydroxide in order to achieve an appealing matte surface. A thin layer of aluminium is removed to create a matte or dull finish.
 - Brightening: the aluminium's surface is smooth with a mixture of nitric and phosphoric acid in order to create a near-mirror finish surface.
3. Mechanical preparation (grinding/brushing): gives a silk or matt appearance and a flat, even surface.
4. Polishing and buffing: removes die-lines, tool marks and surface blemishes, grinding lines and stress raisers. It involves procedures such as shot peening and sandblasting that can improve the aluminium part's fatigue, hardness, resistance and coating adhesion.
5. High finish polishing: mirror finish – usually followed by bright anodizing.
6. *Anodizing*: Aluminum is immersed in an acid electrolyte bath; an electrical current passing through the acid creates in contact

with the material an anodic film. The final product is realized tightly, controlling the coating thickness and surface characteristics.

7. *Sealing*. This process closes the pores in the anodic film, giving a surface resistant to staining, abrasion, crazing and colour degradation (with boiling water or polymers).

Before sealing is also possible to apply some colours in three different ways:

- *Integral Colouring* – It is a process which significantly electrical power, so it is very expensive. This so-called one-step process combines anodizing and colouring to simultaneously form and colour the oxide cell wall in bronze and creates some black shades while being more abrasive resistant than conventional anodizing.
- *Organic Dyeing* – It is a process which involves a small amount of colouring (compared to the other process) and less amount of initial capital, so it is a method relatively inexpensive. The organic dyeing process produces a unique intensity of colour easy recognizable and difficult to create with other paint systems in the market. The variety of colours generated is wide. They can also provide excellent light-fastness and weather-fastness. The structures built with organic dyeing usually have lasted more than 20 years. The colour range can be broadened by over-dyeing the 43 electrolytic colours with organic dyes for a wider variety of colours and shades.
- *Interference Colouring* – It consists of a modification of pore structure using sulfuric acid in order to create colouring shades. At the base of the pore occurs a pore enlargement. Shadows in

a range of red, yellow, blue and green appear with metal deposition at this location. The optical interference and light scattering caused the colours, as with the basic electrolytic colouring process. A greater variety of colours will be produced with further development.

2. Experimental procedure

2.1. Introduction

In this procedure, there will be a study of specimens made on 3D printing that came from a previous work done by Mr. K.J. Moremi for the University of Pretoria [14]. The specimen arrived in a rectangular shape (in a darker colour in **Figure 2.1**)

2.2. Anodizing

The specimen composition given by the work of Mr. K.J. Moremi is confirmed by the analysis of mass spectroscopy (**Table 2.1**). After a quick check of the chemical composition of the alloy of the sample with the Optical Emission Spectroscopy (OES).

<i>Al</i>	<i>Si</i>	<i>Mg</i>	<i>Mn</i>	<i>Cu</i>	<i>Fe</i>	<i>Ni</i>	<i>Zn</i>	<i>Ti</i>
89,48	9,99	0,298	0	0,004	0,16	0,018	0,009	0,008

Table 2.1: Chemical samples composition conducted with spectroscopy

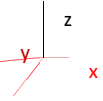
The specimen is cut in a piece of 20x20 mm with a bandsaw at a slow speed (in order not to create any reheating in the cutting zone) (**Figure 2.1**).

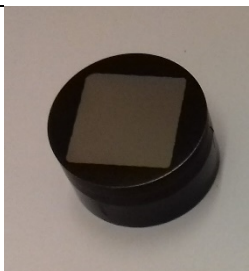


Figure 2.1: Sample arrived from Pretoria (100x40 mm) on the bottom. Sample cut in Jönköping University (20x20 mm) on top

In order to analyse the macrostructure with Light Optical Microscopy (LOM) and a Scanning Electron Microscope (SEM), the samples are mounted in a conductive powder in the three faces directions (**Table 2.2**).

Using Miller's index (**Figure 2.2**), the three vectors are renamed as $\vec{a}_1=x$, $\vec{a}_2=y$ and $\vec{a}_3=z$ (building direction). So surfaces studied are so-called

Name	Miller' index	Surface [mm ²]
XY1 	001	20*20 = 400





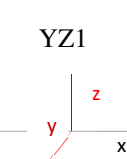

 <p>XZ1</p>	010	$20 \times 5 = 100$	
 <p>YZ1</p>	100	$20 \times 5 = 100$	

Table 2.2: Renamed samples no anodized

$(\vec{a}_1, \vec{a}_2, \vec{a}_3) = (x, y, z)$, and they are the $YZ=(1,0,0)$, $XZ=(0,1,0)$ and $XY=(0,0,1)$.

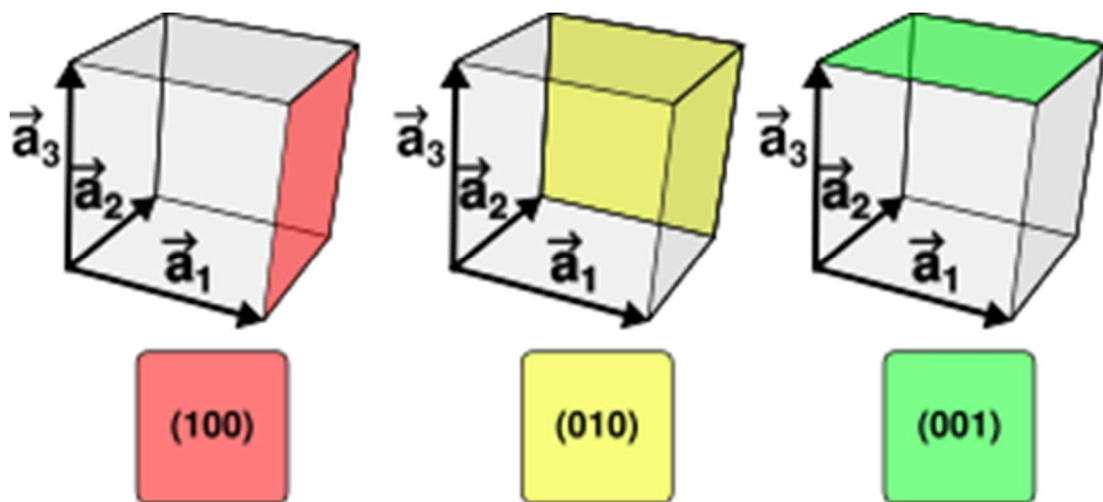


Figure 2.2: Planes defined with Miller's index

Samples candidates for anodizing are connected with copper tape to an electric wire and mounted in a non-conductive resin (*Expofix*); the face exposed is the one anodized, and the resin protects the other surfaces not involved in the process.

Samples not anodized are hot mounted in a conductive powder *PolyFast* is the perfect resin for an SEM microscope because of the carbon filler that secures the conductivity.

According to the standard foundry techniques, all samples mounted into a conductive and non-conductive resin are polished and ground following those eight steps (**Table 2.3**).

The polish machine used in this procedure is the *Tegramin-30* machine (all equipment for metallography comes from *Struers company*), so the last disk's name is given by the industry:

<i>Step n°</i>	<i>Disk</i>	<i>Time [min]</i>
1	320	6
2	500	5
3	800	5
4	1000	6
5	4000	7
6	Largo	7.5
7	Mol	7.5
8	Nap	8

Table 2.3: Grinding and polishing steps

Sandpapers grit size is referred to CAMI Grit designation and not the particles' dimension in millimetres. So the last stages have finer grit than the first one used.

At the end of each step, samples (also the holder) are cleaned with water, ethanol and dried with a combo of compressed air and a ball of cotton wool. The last cleaning phase was done by putting samples in an electrolysis machine in order to remove minor impurities.

Those steps gave, as a result, a glossy surface without any scratches. Surfaces so treated are ready for other studies and processes. A chemical attack was made on XZ1 and the average area of XY1 was calculated with Icy.

Examples of the final result are shown in the following figures (**Figure 2.3** and **Figure 2.4**).



Figure 2.3: Sample mounted in a no-conductive resin



Figure 2.4: Sample mounted in a conductive resin

2.2.1. Anodizing preparation

The anodising process is performed in a bath of H_2SO_4 (sulfuric acid) at a constant voltage of 30 V for 45 mins at $22\pm 1^\circ\text{C}$. As said in 1.2.3 temperature of the bath increase during the process, so some ice cubes are added to a chiller machine in order to keep the temperature constant. Voltage is kept constant using a programmable DC bench power supply (Velleman PS3005D). Between samples and the inert plate is maintained a distance of 20 mm (**Figure 2.5**). The process is done one sample at a time, and the inert plate and clips must be washed carefully every at the end of every 'cycle'. This setup ensures the growth of the barrier and porous layer.



Figure 2.5: Sample during the anodizing process

Prior to anodizing, the samples were ultrasonically cleaned in acetone and ethanol, with immersion times of 3 min.

After anodizing, the samples are washed with distilled water and dried with a cool air stream and dried up in the oven at 50°C for 45 min (**Figure 2.6**).



Figure 2.6: Oven for porous sealing

The oxide layer is checked with a coating thickness measuring instrument. According to Fischer Technologies and DIN EN ISO 2360, for 'Paint, lacquer or plastic coatings on non-ferrous metals, anodized coatings on aluminium and electrically conducting coatings on electrically non-conducting carrier materials' the right instrument for thickness measuring is based on eddy current method (**Figure 2.7**)[32].

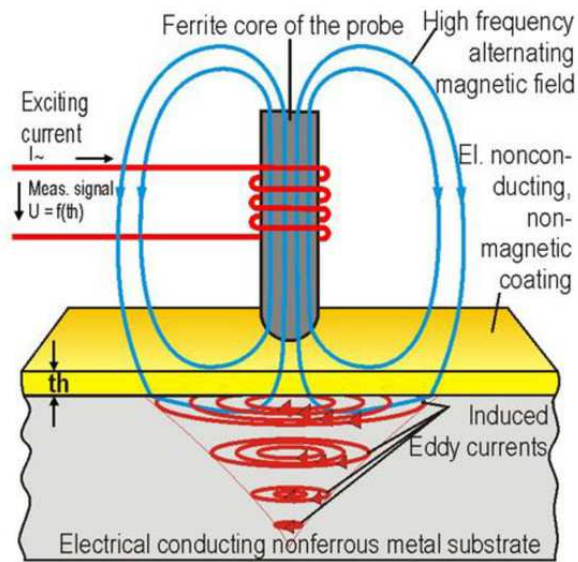


Figure 2.7: Eddy current method scheme on Fischer Isoscope

Eddy current in based material is created by the primary field generated from the excitation of the probe. The weakness of the primary and secondary field is read by the instrument as the distance between the probe and the base material (so-called *coating thickness*).

According to [33], thickness measures in 001 and 010, and 001 should be the same.

2.3. Hardness

In order to study the hardness of the anodized layer, anodized samples are cut in half (in the direction of anodized growth) and embedded in a transparent resin in order to indi

The microhardness is based on the Berkovich tip (**Figure 2.9**), a helpful nanoindenter for thin film.

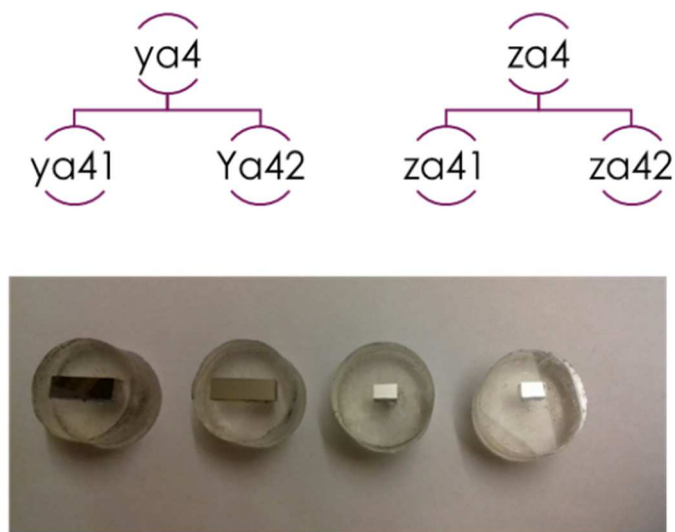


Figure 2.8: Cross section of samples Ya4 and Za4 polished, into resin

The force applied is 20 mN for 10 min at different points of the oxide layer (in order to have a complete sample scenario of oxide hardness).

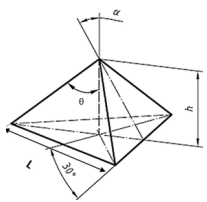
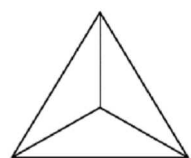
<i>Feature</i>	<i>Size</i>	<i>Front view</i>	<i>Top view</i>
Semi-angle (α)	65.3 °		
Apex half angle(θ)	76.9°		
Tip radius	200nm		
Height (h)	1 μ m		
Base length (L)	7.52 μ m		

Figure 2.9: Characterization of Berkovich tip

2.4. Wear test

A motion between a surface and a material or substance creates damage called *wear*.

The tribological behaviour of anodized coatings was evaluated on a ball-on-disc tribometer (CSM Instruments, now Anton Paar, Neuchatel, Switzerland) under dry sliding conditions. (Figure 2.10)[34]

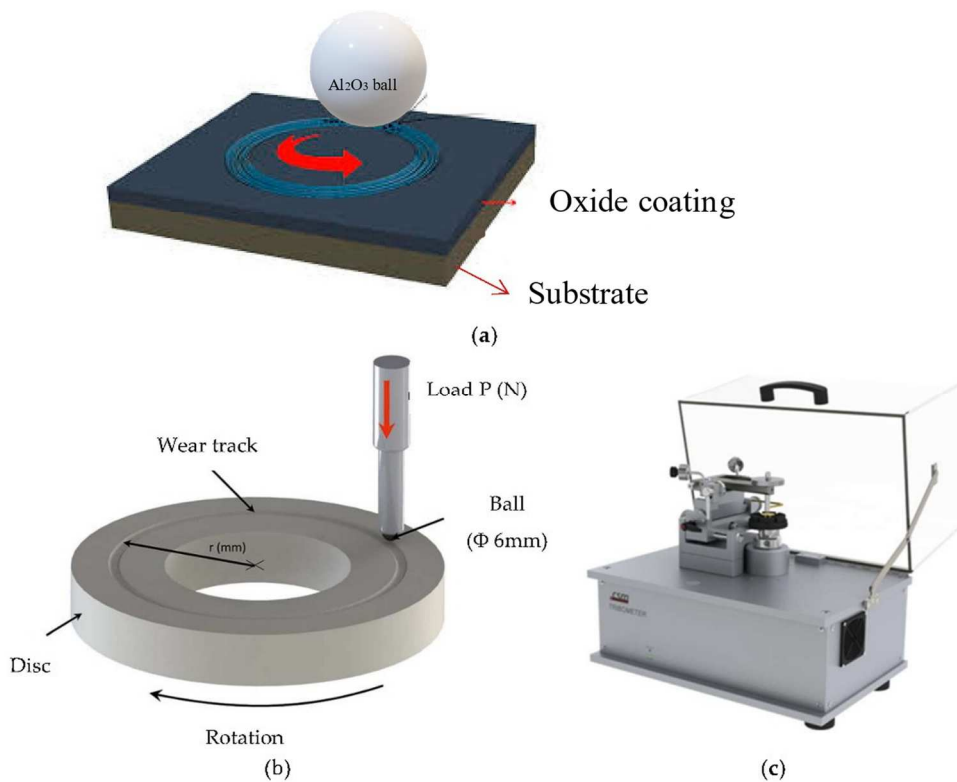


Figure 2.10: Ball-on-disc configuration friction test (a), (b) +CSM apparatus (c)

The candidates of this test are samples in XY direction because of their dimension, which allows a proper work of machine test.

Al system is levelled and checked with a comparator (Mitutoyo, Absolute, Digimatic Indicator ID-U) placed in the same position in which later a static partner in Al₂O₃ with ball shape with radius dimension of 6mm.

Machine setup is:

- temperature of 23±1°C
- humidity at 19±1%
- acquisition frequency of 10 Hz
- normal load of 1N

During the test, only the anodic layer was worn out by performing 35 laps with a linear speed of 3cm/s.

After tests, the surface profiles of the wear tracks were measured while using a stylus profilometer. The wear rates of tested coatings were calculated using the following equation:

$$Wr = \frac{V}{L * Load} \quad \text{Formula 2.1 Wear rate formula}$$

Where:

- V is the wear volume loss also calculated in mm³ as:

$$V = A * 2 * \pi * r \quad \text{Formula 2.2 Volume formula}$$

- A is the area of the hole (given by the roughness tester in μm²)
- r is the radius in mm
- L is the sliding distance, also calculated as:

$$L = 2 * \pi * r * N \quad \text{Formula 2.3 Sliding distance}$$

- N is the laps number

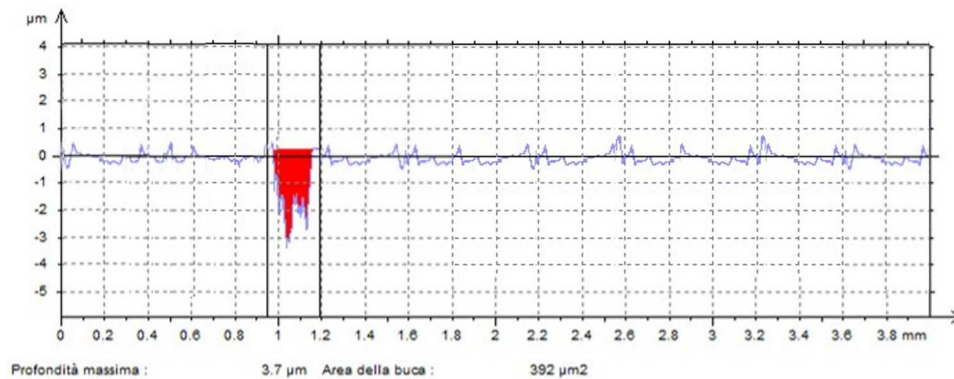
So is also easy to calculate as:

$$Wr = \frac{A}{N * Load}$$

Formula 2.4 Wear rate simplified formula

The software connected to the roughness tester (TalyProfileLite 3.1.0) gives information regarding the hole area (in red colour in **Figure 2.11**). Around the hole area is possible to observe the roughness of the surface and edges of the track.

Figure 2.11: profile after wear test



2.5. Corrosion and EIS

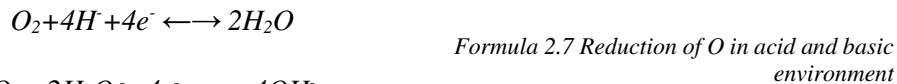
Anodized samples, so done, are ready for corrosion test.

This work is referred to *wet corrosion*, which means that samples are immersed in a liquid bath (Cl). Dried corrosion (thermal oxidation) is also used but not so common because it works at higher temperatures.

Wet corrosion is a result of RedOx reactions from the reduction of the cathode and oxidation of the anode.



The reduction reaction is correlated to the corrosive environment and is possible to have a reduction of hydrogen, oxygen (in acid or basic environment) or other metallic ions:



The number of electrons produced during the anodic process is the same as the consumed ones in the cathodic process. Migrations of electrons from the anode to the cathode induce a current flow in the opposite way inside the metallic conductor. Meanwhile, there is also anions migration inside the bath: negative ions move from the solution to the anode and balance positive ions from oxidation semi-reaction, and positive ions move from the bath to the cathode and substitute cations consumed or balance anions generated. Migrations of ions generated in the bath a current from the anode to the cathode.

All those currents in a corrosion cell generate an electric circuit. Equilibrium is reached when anode and cathode currents are the same.

Applying Faraday's law is possible to determine the corrosion current: the amount of corroded metal (from the anode) that passes through the bath in a

specific range of time. Corrosion speed is proportional to the current and is the inverse of the area exposed to the corrosive attack.

So, electrochemical impedance spectroscopy *EIS* is performed using a three-electrodes arrangement. Anodized specimens (one at a time) are immersed in a bath with 3 wt-% NaCl, with a reference electrode in Ag/AgCl and a counter in Pt (**Figure 2.12**).

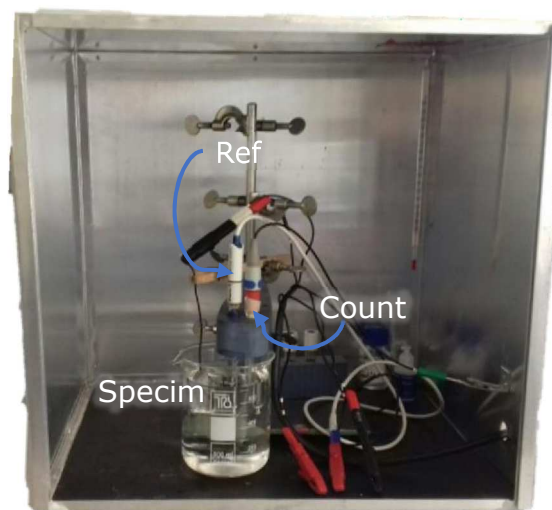


Figure 2.12: EIS setup

The frequency ranged $10^5 - 10^{-2}$ Hz with 36 points in 5 dC, turbulence at 15 mV, current range $10-10^{-2}$ mA and voltage at $\pm 0,6$ V. Electrochemical measurements are collected during 24 hours of immersion (9 cycles and 10 mins of pause between each cycle).

The EIS gives as results data that should be re-arranged and studied with ZSimpWin software. This software is used for electrochemical measurements and gives back the impedance data. [12]

ZSimpWin shows data as points that must be fitted into the best circuit given that can be able to represent the phenomena. Studies were done for anodized

casting aluminium (in the same conditions of this work and for long immersion time in the electrolyte) suggest that $R(RQ)(RQ)$ (**Figure 2.13**) or $R(Q(R(QR)))$ (**Figure 2.14**), can be a solution; so those two were the starting point for the research of the right one.

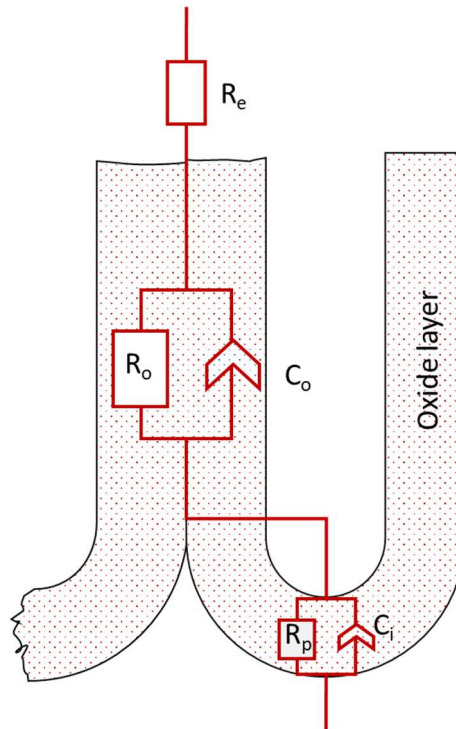


Figure 2.13: Circuit in porous section $R(RC)(RC)$

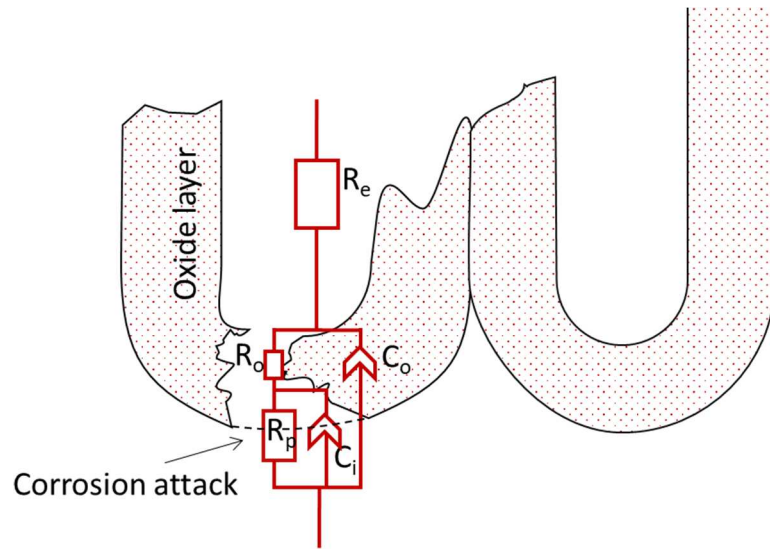


Figure 2.14: Equivalent circuit $R(C(R(CR)))$

In order to clarify the equivalent circuit, the components are named:

Name	Equivalent component
R_e	Resistance of the electrolyte
R_o	Resistance of oxide layer
R_p	Resistance of polarization
C_o	Constant phase element for oxide layer
C_i	Constant phase element for the interface

Table 2.3: EIS equivalent circuit members

Corrosion processes have a response in an impedance measurement. If corrosion occurs underneath coatings, electrons are transferred between molecules and metals in the corroding system. This charge transfer can be studied with standard electronic entities such as impedance.

The proper circuit interpolation of point gives a Bode diagram: on x-axis is possible to find the range of frequencies (Hz), on y-axis, impedance in the modulus [$\Omega \cdot \text{cm}^2$] and angle (deg), an example of obtained Bode diagram is showed in the **Figure 2.15**.-During immersion time, the phase angle increase and the total impedance modulus decrease.

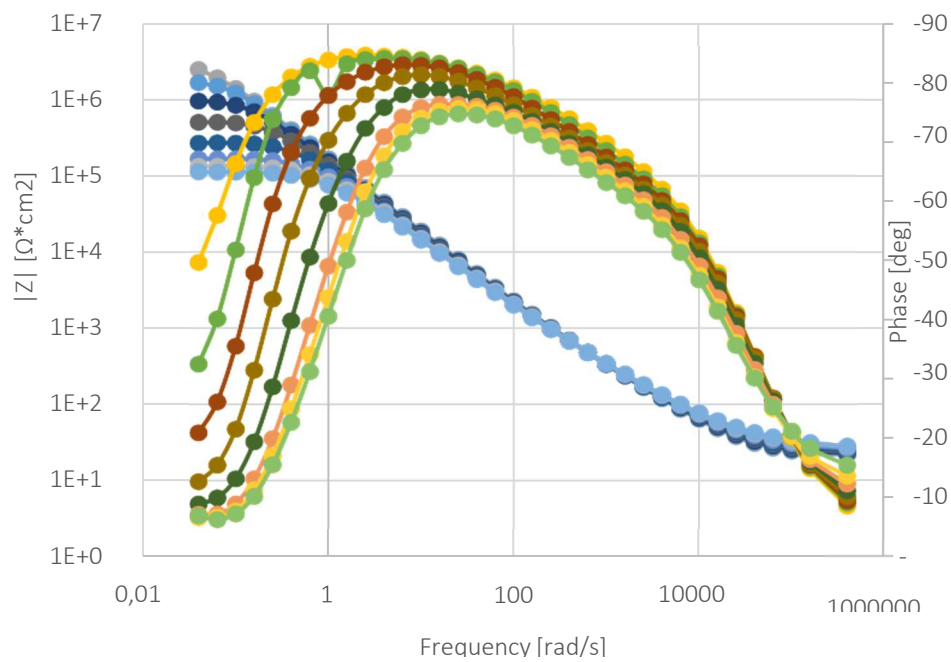


Figure 2.15: Example of Bode diagram obtained after EIS measurements in 9 cycles in 24 hours

The corrosive attack will also be visible, observing the decrease of the value of R_p during the time of immersion.

3. Results

3.1. Chemical composition

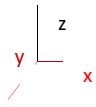
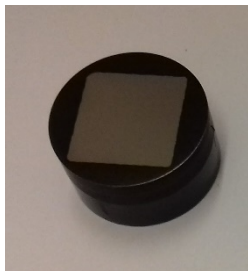

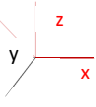
The chemical composition of samples is determined using spectroscopy in weight percent

<i>Al</i>	<i>Si</i>	<i>Mg</i>	<i>Mn</i>	<i>Cu</i>	<i>Fe</i>	<i>Ni</i>	<i>Zn</i>	<i>Ti</i>
89,48	9,99	0,298	0	0,004	0,16	0,018	0,009	0,008

Table 3.1: Chemical composition conducted with spectroscopy (%wt.)

3.2. Qualitative and quantitative analysis

As said in the experimental procedure' paragraph, samples were cut in three different directions and renamed as follows in **Table 3.2**:

<i>Name</i>	<i>Miller' index</i>	<i>Surface [mm²]</i>	
XY1 	001	20*20 = 400	 
XZ1 	010	20*5 = 100	

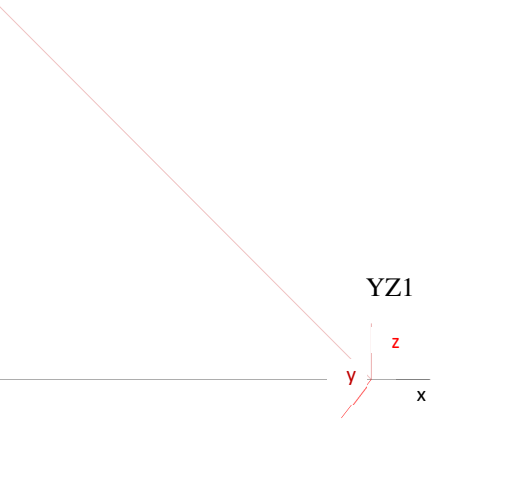

	100	$20 * 5 = 100$	
--	-----	----------------	---

Table 3.2: Renamed samples no anodized

3.2.1. Macrostructure analysis

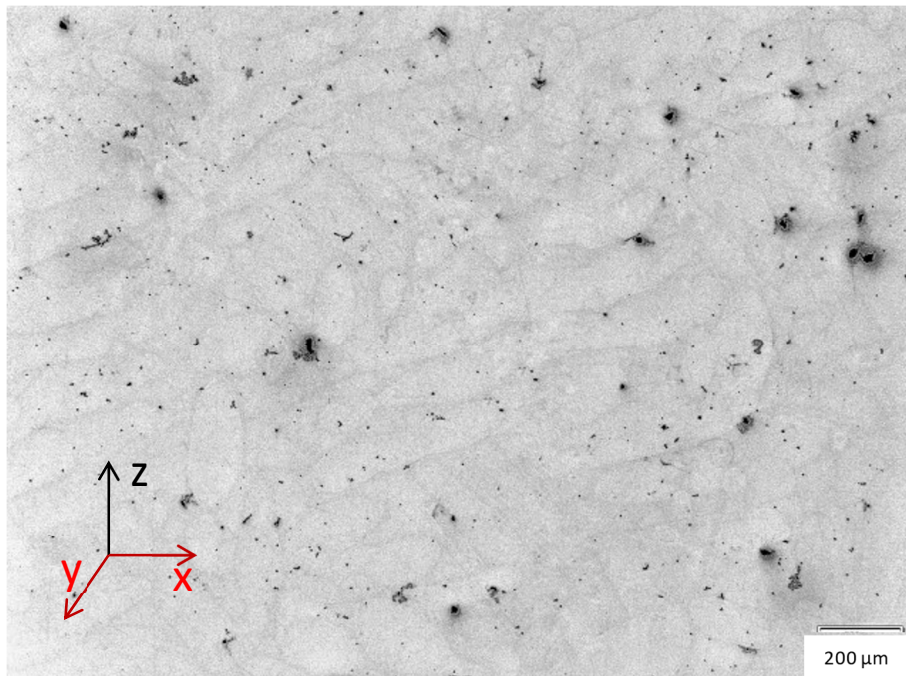


Figure 3.1: Micrography of XY1 sample

In **Figure 3.1**, it is possible to observe the typical top structure made by the laser beam. Dark spots evidence the presence of porosity that can be created by the SLM process. Because of SLM process is not a homogeneous process, some particles might not be melted by the laser, so during the cleaning process, those ones detached from the sample and created some empty spaces. According to Brandl [3], the presence of porosity detracts mechanical properties and fracture behaviour. By the way, the size of pores can be

controlled layer by layer during the SLM process, checking all process parts. For instance, in order to increase density is possible to act on scan speed and higher laser power.

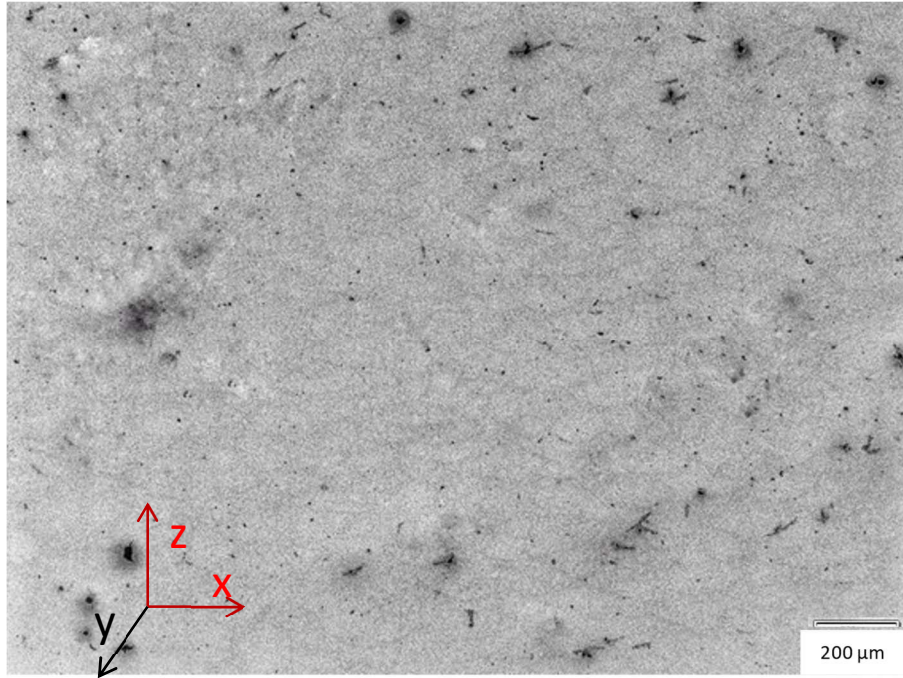


Figure 3.2: Micrography XZ1 sample

In **Figures 3.2** and **3.3**, it is clear the ‘fish scale’ structure was obtained in the parallel plane of building direction after polishing and the cross-section of the specimens.

But in order to investigate the microstructure better using scanning electron microscopy, XZ1 etched with Keller’s reagent:

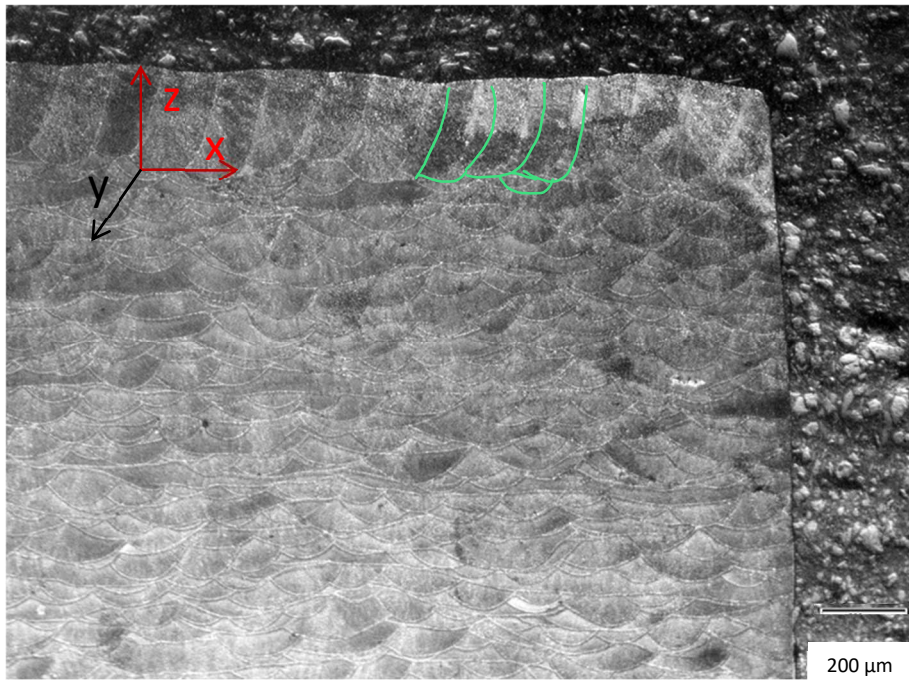


Figure 3.3: XZ1 after Keller' etching – overlapping detail (in green)

In XZ (and also YZ) plane possible observe overlapped melt pools due to the subsequent layers (**Figure 3.3**).

Black areas in **Figures 3.1, 3.2** and **3.3** are porosities. This phenomenon is expected because of the additive manufacturing process.

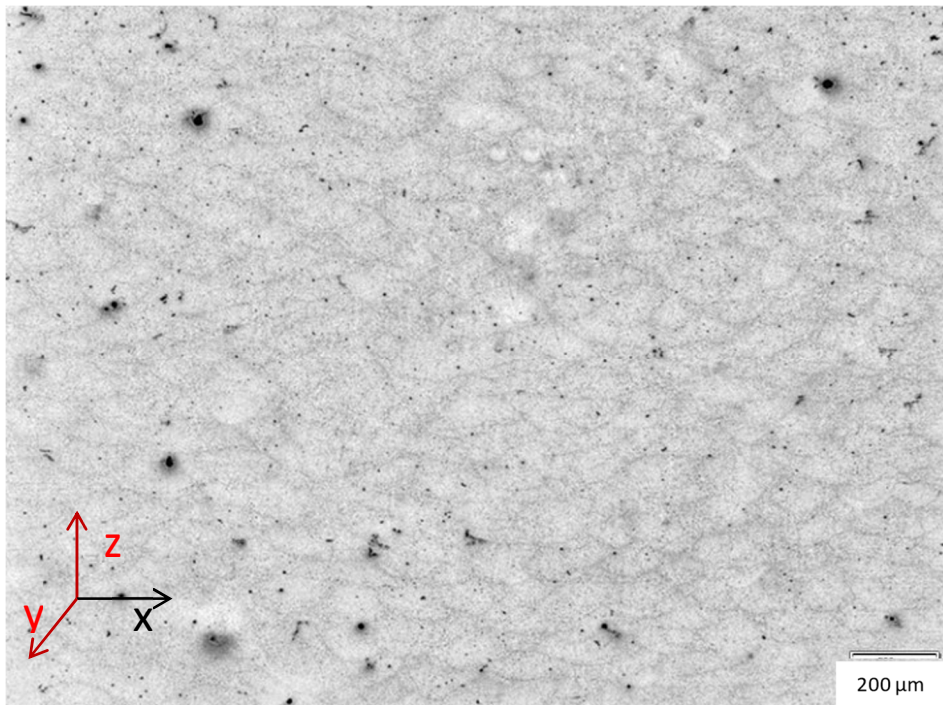


Figure 3.4: YZ1 sample

It is possible to reduce the number of tests, approximating YZx and XZx. This is due, for instance, to the same area of Al-scales of the two faces.

Areas of every scale are calculated with Icy software and with ImageJ.

<i>Name</i>	<i>Mean scale area [μm^2]</i>
XZx	4855±0.6
YZx	4836±0.6

Table 3.4: Scale areas of Al pool in laterals (XZ1 and YZ1)

3.2.2. Microstructure analysis

Higher magnification images were obtained using SEM.

Proceeding with the analysis of lateral XZ1, it is possible to observe the three zones: the finer one, the ‘heat effected’ one (HAZ) and the coarse quite visible also at just 10 μm (**Figure 3.5**):

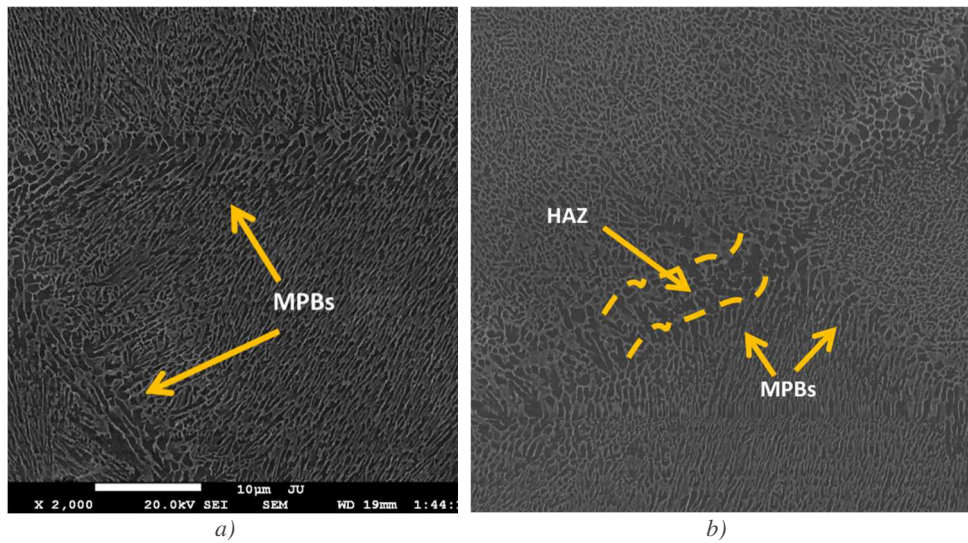


Figure 3.5: a) Melting pool borders and b) HAZ of XZ1

The centre of the melt pool harbours fine Al cells. The structure is coarser toward the melt pool borders. So next, MPBs Si-network is broken up and created the so-called HAZ. The creation of HAZ happens when the material is affected by the heating generated by the laser passing and the creation of the adjacent melt pool.

The Energy Dispersive Spectroscopy (EDS) also bolsters that the visible matrix is in Si (**Figure 3.6**).

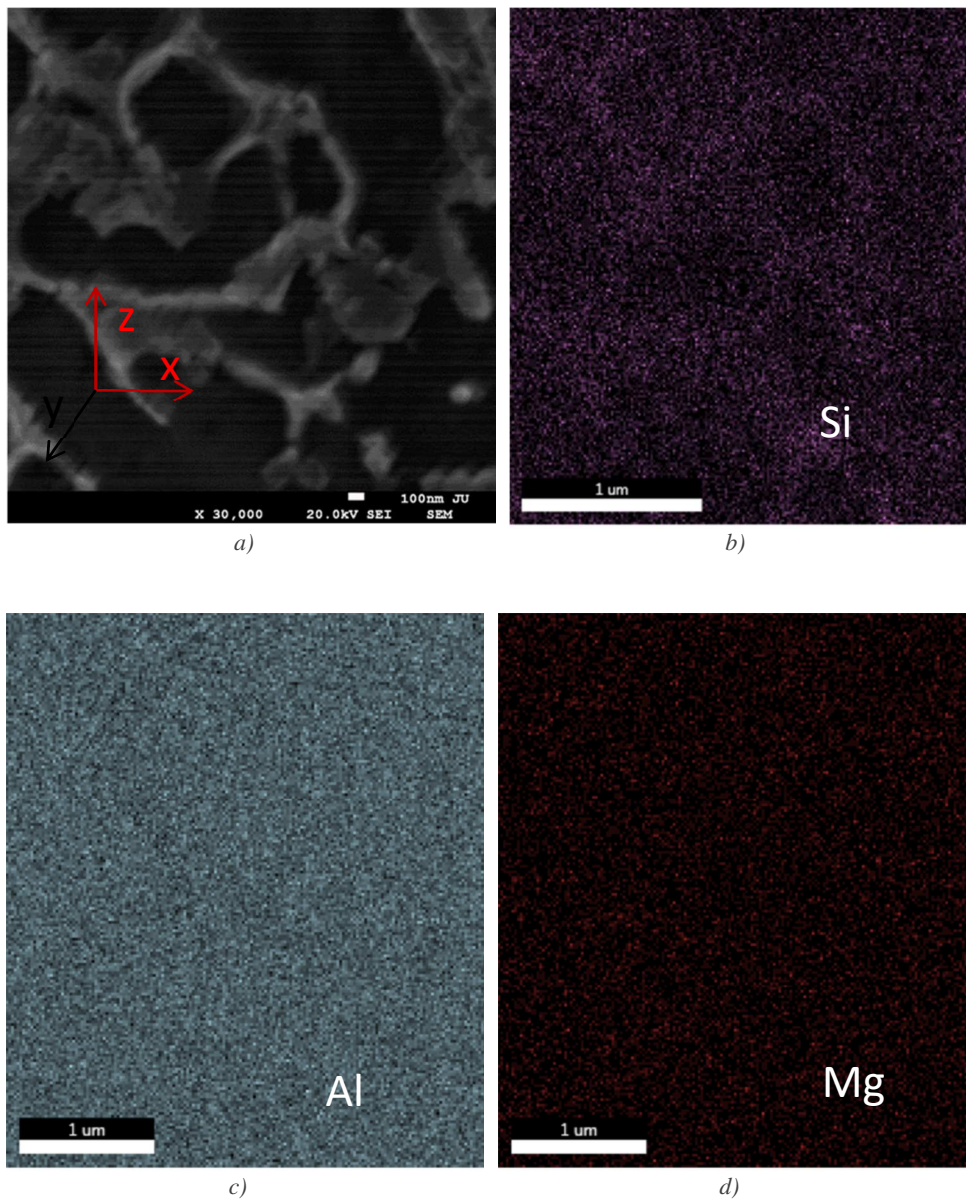


Figure 3.6: Surface parallel to the growth direction (XZ1) a) after EDS mapping: Si in purple matrix b). c) and d) reveal a uniform distribution of Al and Mg

SEM and Energy Dispersive Spectroscopy (EDS) also confirmed the structure of the top surface (**Figure 3.7**):

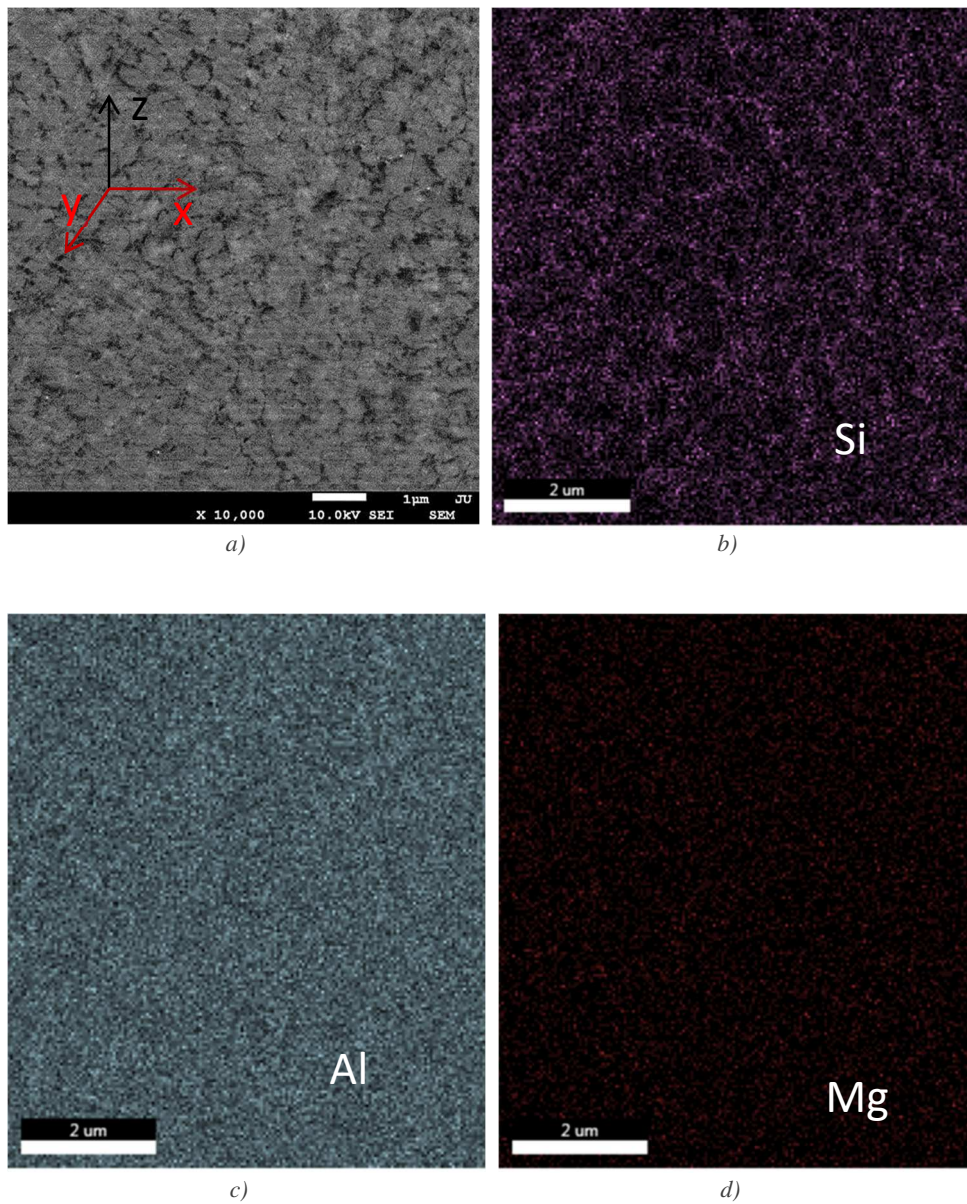


Figure 3.7: Surface perpendicular to the growth direction (XY1) a) and after EDS: Si in purple network b) c) and d) reveal a uniform distribution of Al and Mg

Higher magnifications (also using a scale of 1nm) prove, with ImageJ, that lateral samples are identical in terms of Al-grain area (XZ1 and YZ1 with $4850 \pm 0.6 \mu\text{m}^2$), different from XY1 at $63000 \pm 1000 \mu\text{m}^2$. This also indicates

a finer distribution of Si in the XY direction, but irrelevant enough because of the dimension.

Qualitative and quantitative analysis verified what was found in the literature [12]: the presence of a homogeneous amount of Al and a continuous and finer network of Si-particles for the longitudinal section (**Figure 3.7**) and fibrous for the traversal one (**Figure 3.6**).

Thanks to the etching, the structure of side faces was quickly visible just using not higher magnifications in optical [22](**Figure 1.11**).

Using the same alloy and going back to a traditional casting process, the light optical microscope (LOM) reveal the same magnificent structure change (**Figure 3.8** vs **Figure 3.10**).

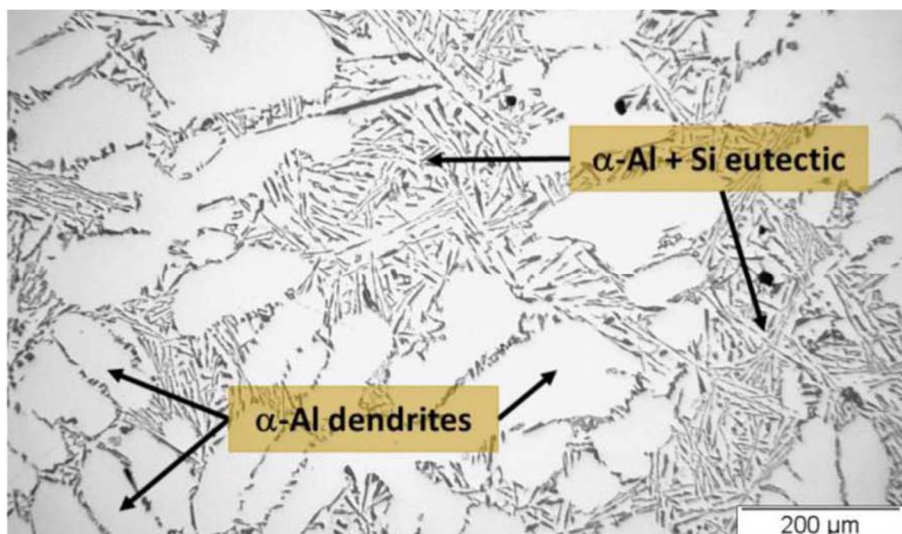


Figure 3.8: Optical image of a region in the surface of the cast alloy AlSi10Mg [35]

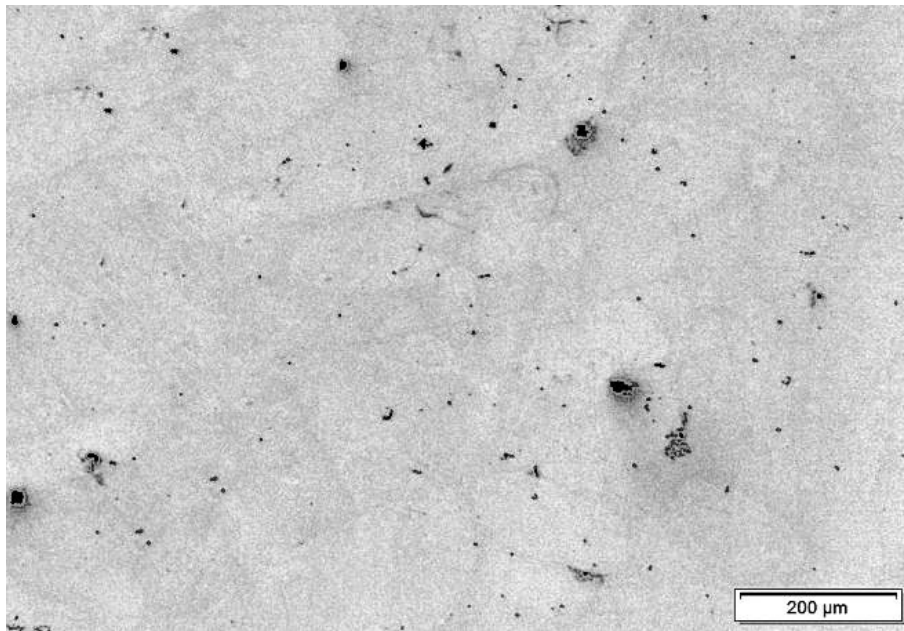


Figure 3.9: Optical image of the surface parallel (XY) to the building platform of SLM AlSi10Mg

For cast alloys, needles of silicon are visible at lower magnification (**Figure 3.8**). This is due to the hypoeutectic composition, which leads to the formation of primary α -Al dendrites followed by the solidification of eutectic α -Al + Si.

Higher magnifications in the scanning electron microscope (**Figure 3.10**) show better silicon needles in a casting process (for instance, in the direction perpendicular building direction). Silicon is quite big and without any creation of a network, as is visible in the SLM process. [5]

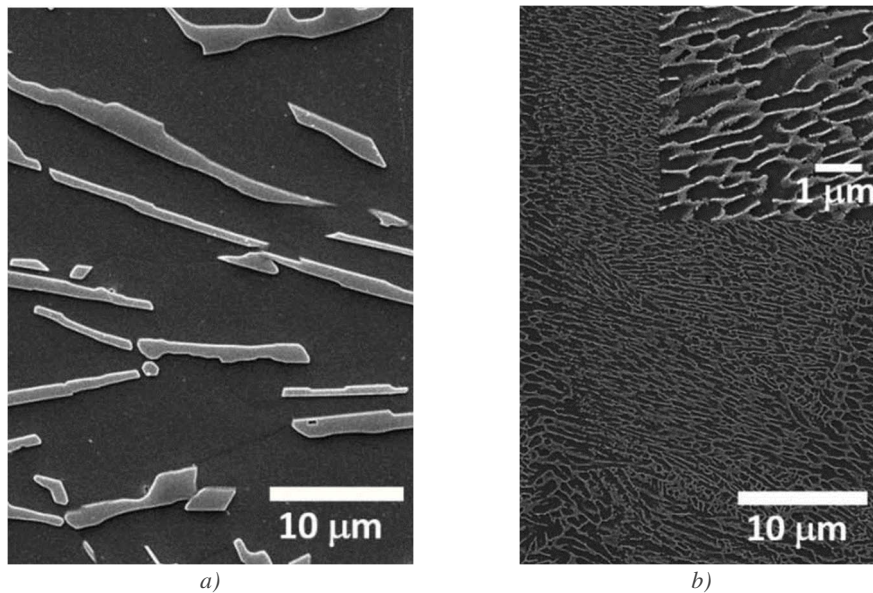


Figure 3.10: AlSi10Mg in XY plane a) cast b) in AM-SLM at the same magnification. In white, the Si phase [35]

The tracks created with selective laser melting (SLM) process are visible in **Figure 3.1** and **Figure 3.2**, but silicon is not so visible. For the same scale of $10\ \mu\text{m}$ silicon needles much more enchanted in the cast process (**Figure 3.10a**) compare to the same alloy but made in SLM (**Figure 3.10b**).

Last but not least, at higher magnification and with the help of SEM, the cast alloy can be observed in the large Si needles, while the silicon phase in SLM is much more dispersed and finer within the matrix and forms a 3-D network that encloses the α -Al cellular cells (visible in both directions: **Figure 3.1** and **3.2**).

As mentioned before, the presence of porosity is an issue that can be controlled with process parameters; but parameters are also relevant for observations at higher magnifications. The ultra-rapid solidification (10^6 – 10^8K/s) allows for an excellent cellular microstructure. [36]

Due to the supercooling rate, silicon precipitates and forms an ultrafine network structure; moreover, in cast process, silicon lamellar.

Parameters mentioned before, affecting the cooling rate and diffusion rate, also affect the solute concentration of Si into the Al.

4. Anodized samples results

4.1. Anodization

The treatment conducted as explained in the §2 on the two faces in thirteen samples renamed in order to simplify the study (**Table 4.1**).

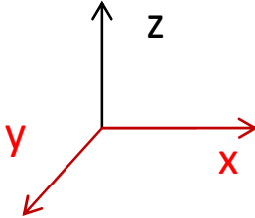
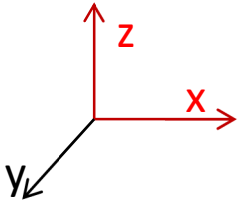
<i>Name</i>	<i>Miller' index</i>	<i>Surface [mm²]</i>	
(X)Ya1	001	20*20 = 400	
(X)Ya2			
(X)Ya3			
(X)Ya4			
(X)Ya5			
(X)Ya6			
(X)Ya7			
(X)Ya8			
(X)Ya9			
(X)Za1	010	20*5 = 100	
(X)Za2			
(X)Za3			
(X)Za4			

Table 4.1: Renamed anodized samples

After a few seconds of immersion into the H_2SO_4 bath, the current density of both sides stabilized over the time (**Figure 4.1**); this indicates that in the first stage of the anodization, there is the creation of the oxide layer; after this ‘barrier’ the porous grow with a stable current (**Figure 1.17**)

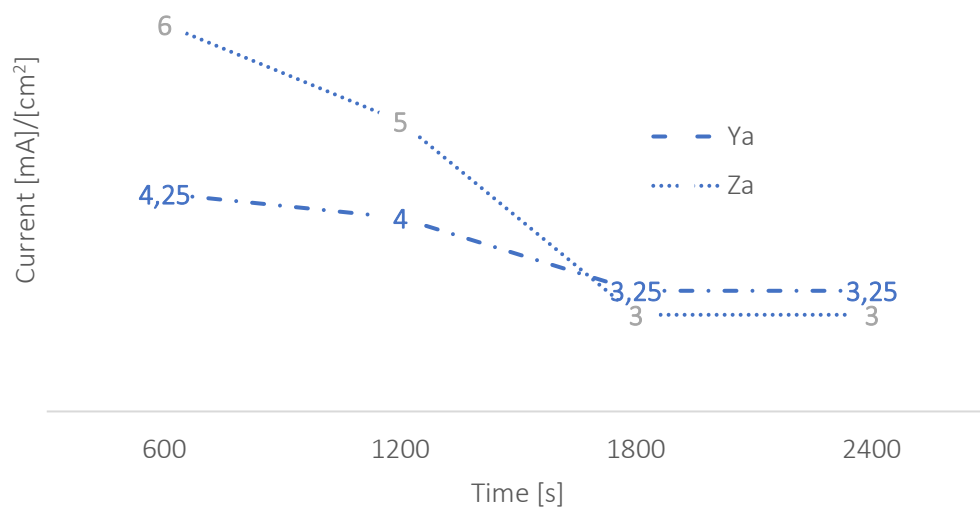


Figure 4.1: Time - Current density

In **Figure 4.1**, it is possible to see how the current density at the first stage is higher in (X)Za samples than in (X)Ya ones, and here there is the initial oxide barrier layer formation. The negative slope indicates pores formation, and then after 30 minutes, the situation switches, and the result is a steady growth of anodic aluminium oxide.

At the end of the anodizing process, a check of anodize thickness was conducted with ‘Eddy current method’.

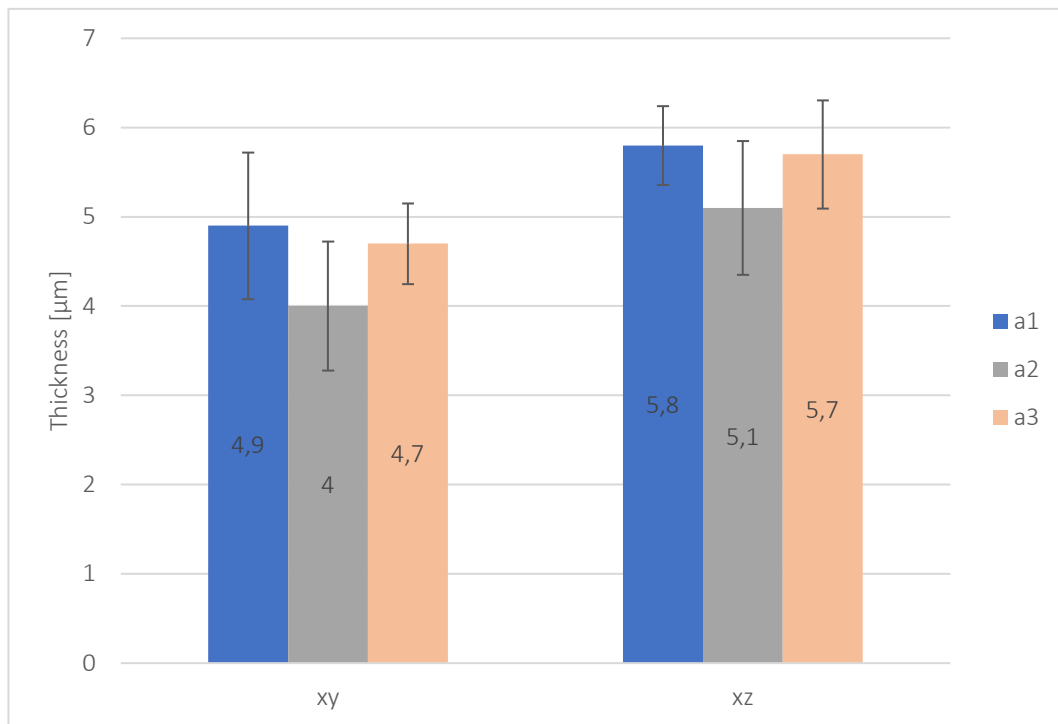


Figure 4.2: Thickness [μm] of the anodized coating measured with Eddy current method

The **Figure 4.2** shows an average thickness that is a bit different between the samples. A variation of $\pm 1 \mu\text{m}$ between the two oriented samples, is observed. The reason is that the structure macrostructure saw in chapter 3.2.1. The melt pool border (MPB) has a cooling rate lower than bulk material in melt pool (MP), and so a coarser structure. In the direction parallel to the building platform, the oxide layer has much more probability of encountering the Si than in the direction perpendicular to the building platform because the bulk material has a more homogenous Si network; this also means that the oxide front is slowed by that (**Table 4.2**). Thus the required electric field strength is higher in XY samples also because Si is a semiconductor and might be partially anodized at a lower rate. On the other hand, XZ-YZ samples have, in general, a lower electrical field strength for anodizing

because of the presence of more MPBs per surface than XY-oriented ones.
[12]

Because of the operative conditions of all samples are identical, the variation in layer thickness can be attributed to sample preparation during polish. Different additive manufacturing layers can be involved, so the layer thickness can vary between samples with the same orientation.

Compared to an anodized sample made by casting the same alloy, oxide layer growth has a slower rate.[12]

<i>SLM XY</i>	<i>SLM XZ</i>	<i>Cast alloy</i>
0.108±0.02	0.12±0.01	0.37±0.03

Table 4.2: Oxide growth rate during anodizing of specimens (in H2SO4 electrolyte) in $\mu\text{m}/\text{min}$ [12]

Due to the Si network created in AM samples, the oxide front during the anodization is obstructed, so the growth rate is more or less four times slower. On the other hand, the thickness is homogeneous, even if it is thinner.

The oxide layer is not clear just watching on top view, so a cross-section will be executed in order to check the thickness measured and to observe the fibrous structure typical of this process.

Samples were cut in cross-sections as follows and mounted in resin (to help visualize the oxide layer **Figure 4.3**) and analyzed with the LOM (**Figure 4.4** **Figure 4.5**).

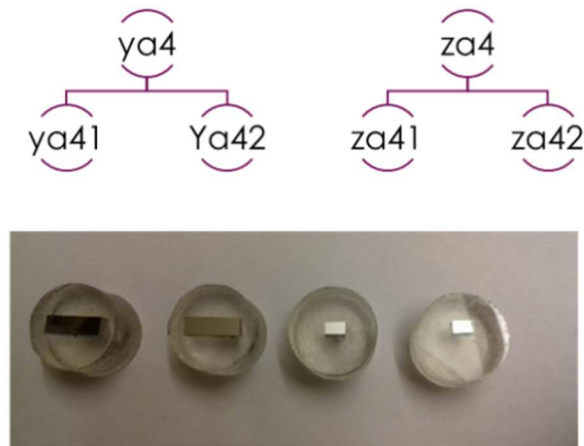


Figure 4.3: Cross section of samples Ya4 and Za4 polished into resin

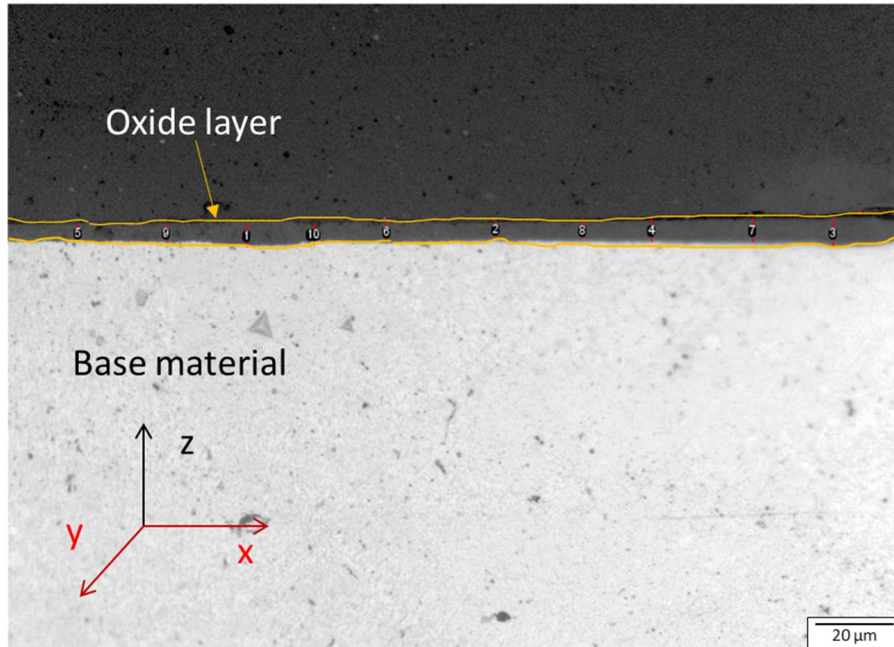


Figure 4.4: Cross section of (X)Ya4 after anodizing and some values of oxide thickness

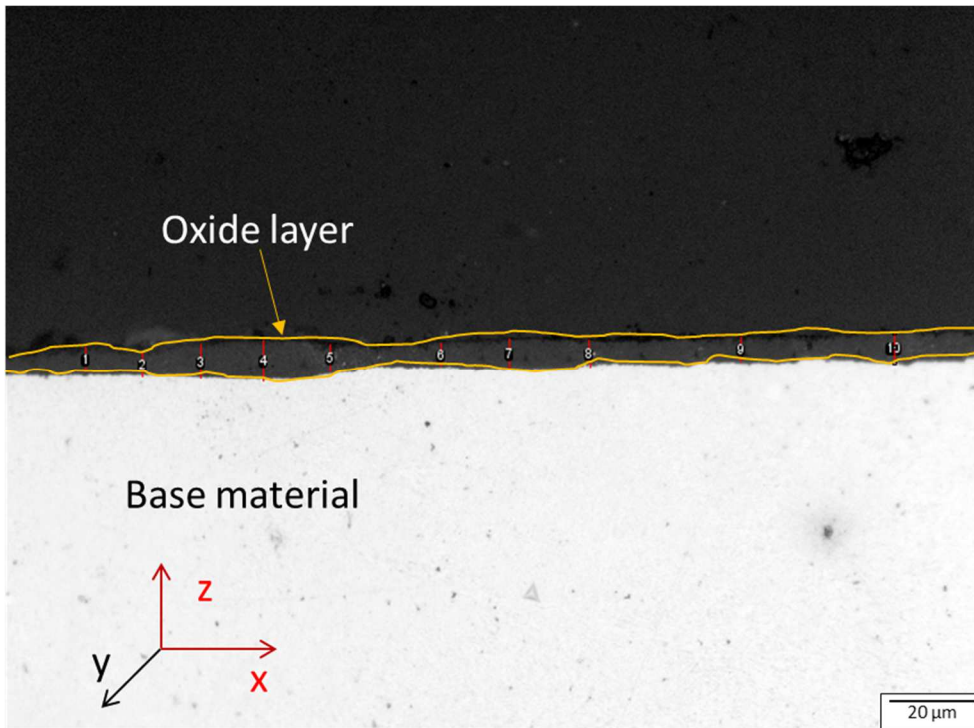


Figure 4.5: Cross section of (X)Za4 after anodizing and some values of oxide thickness

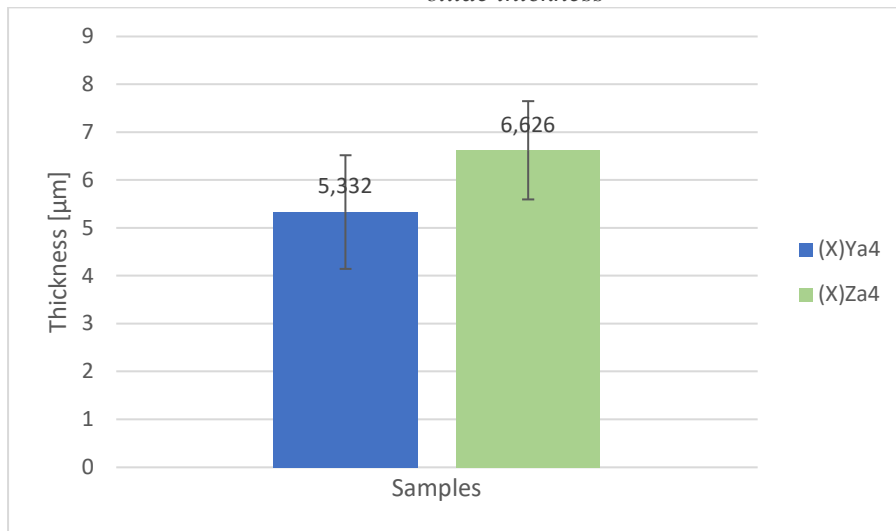


Figure 4.6: Thickness [μm] of anodized coating with cross-section method

In **Figure 4.4**, it is possible to observe a cross-section of the (X)Ya41 sample; in **Figure 4.5**, it is possible to observe the (X)Za41 section. For each sample, ten areas have been analyzed to obtain **Figure 4.6** and confirm results found with Eddy currents about the difference of the oxide layer thickness in the same sample and between the two specimen sides.

Small triangles are the results of a Berkovich indentation that will be commented on later.



Figure 4.7: AlSi10Mg made by casting cross section, after 20 min of anodizing[35]

After just 20 mins of anodizing, the same alloy, made with cast process, in cross-section, showing a thicker layer than samples made by additive manufacturing. It is also quite clear the presence of Si-needles interrupted the growth of the anodic oxide layer, while in the area of second-phase particles free is quite homogeneous. [1].

The growth of the anodic layer has uniform thickness and minimum defects thanks to the presence of a fine Al cell (like in samples made by additive manufacturing). [37]

Sectioned samples also confirm the presence of elements discovered after anodizing with SEM in the top view:

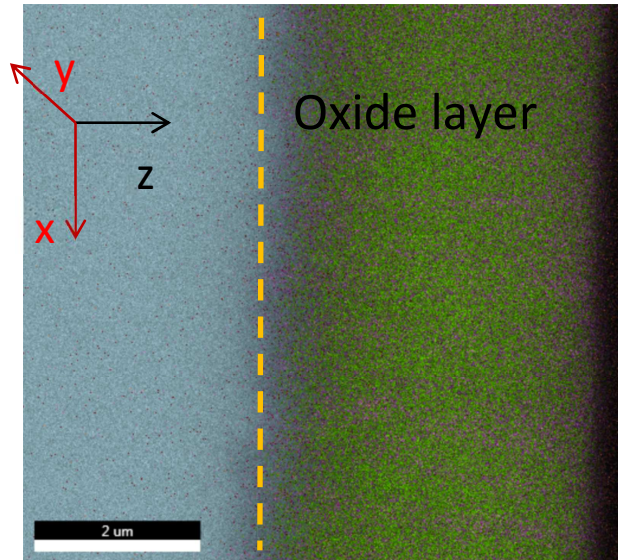
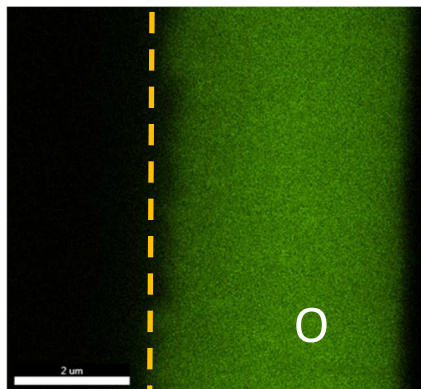
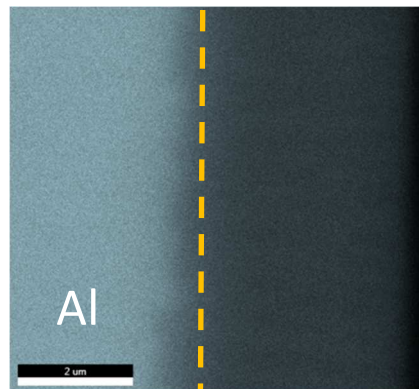


Figure 4.8: Base material (in blue), the oxide layer on lateral. EDS mapping of a cross section of perpendicular section.

Figure 4.8 confirms the presence of the intact base Al material (prevalent Al, indicated with blue colour) and the formation of the oxide layer, with, of course, the huge presence of oxygen.



a)



b)

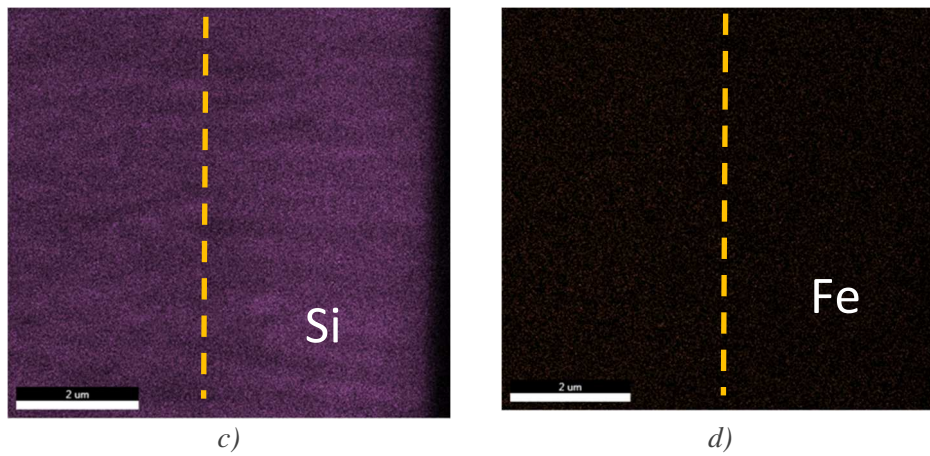


Figure 4.9: EDS mapping highlighting the presence of O, Al, Si and Fe in the oxide layer of Ya4 sample

Figure 4.9 confirms the presence of O (much more in the oxide layer, as expected), silicon is still well distributed, as also the small amount of Fe (so it confirms also that no FeO was created during the anodizing process). Sometimes the presence of porosity can modify the composition of the base material during anodizing, so as **Figure 4.10** shows, some oxide is created outside the common oxide layer.

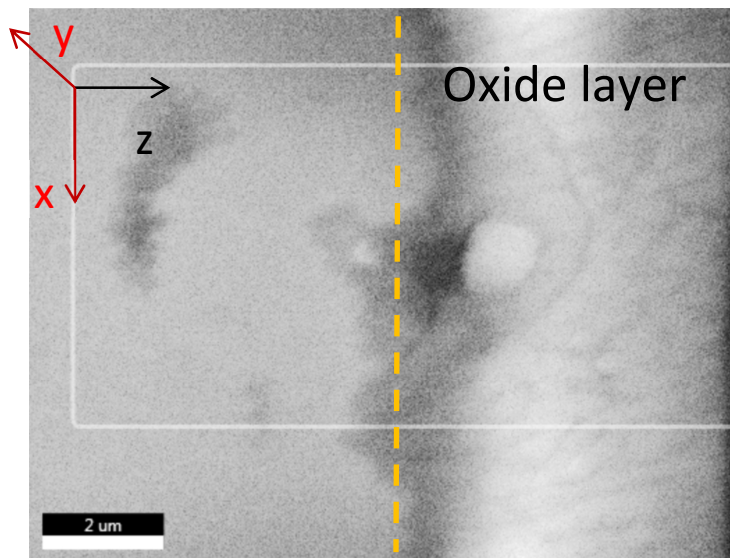


Figure 4.10: EDS mapping, cross section of perpendicular surface (Ya4 sample), highlight a crack

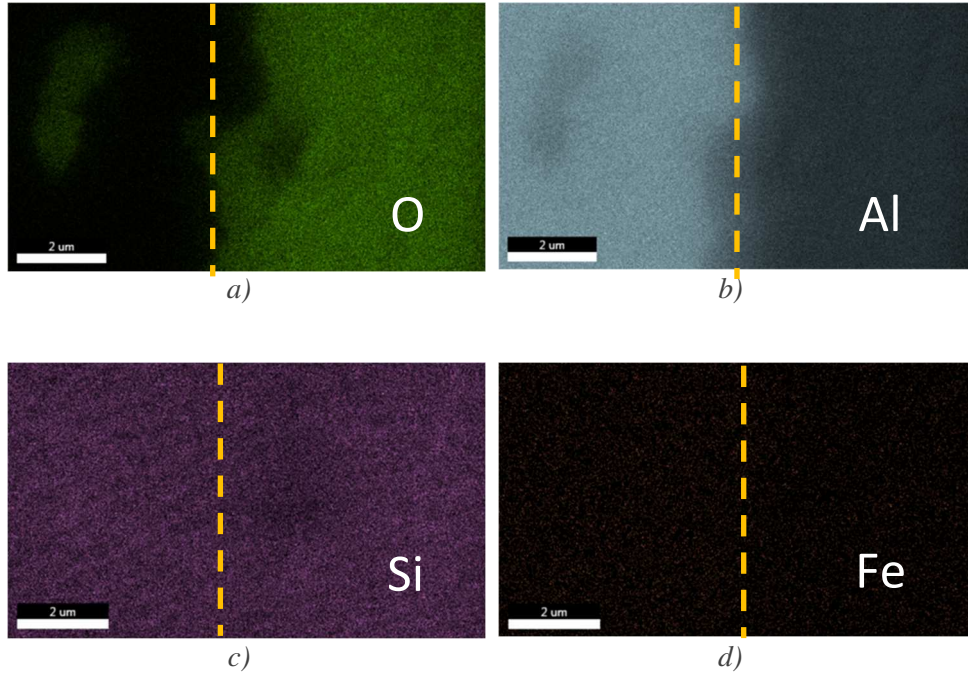


Figure 4.11: EDXS on a cross-section closer to the presence of a crack

Porosities usually are located inside MPs or were also detected along the boundary of consecutive layers or along the interference adjacent between scan tracks. At the interference between the already solidified substrate and melting pool, gas porosities nucleated at the melting front can easily escape from MPs [38] but [39] the pores, due to the gas entrapments, remain in the inner part of MP or at its side because they don't have enough time to escape prior being entrapped to the solidification front itself.

Figure 4.11 a) and b) showed the formation of the AlO inside the material, also responsible for the surface crack.

Roughness samples after anodizing and before corrosion are so analysed. Trials indicate an average of $0.38 \pm 0.2 \mu\text{m}$ of roughness.

4.2. Hardness and wear test

Berkovich hardness test is conducted on the oxide layer using a Micro Materials NanoTest Vantage equipped with Berkovich indenters in different points of the cross-section samples with a significant distance in between (so it was possible to avoid different phenomena such as creeping):

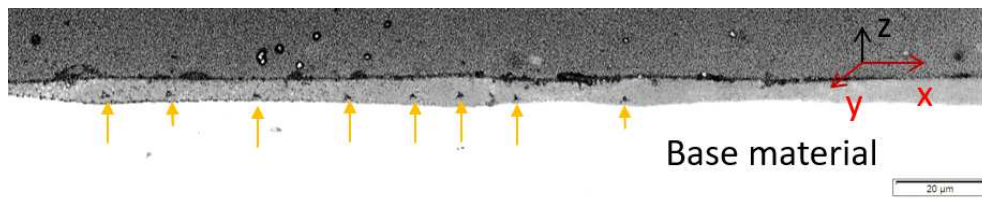


Figure 4.12: Berkovich imprints on oxide layer (Ya42)

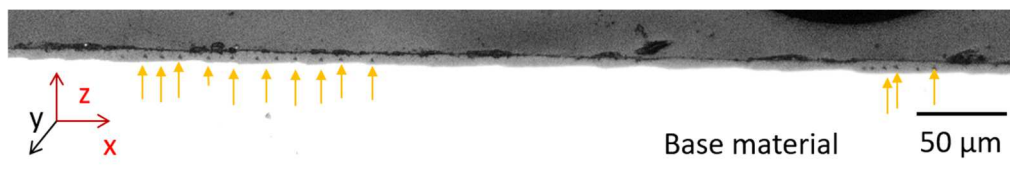


Figure 4.13: Berkovich imprints on oxide layer (Za41)

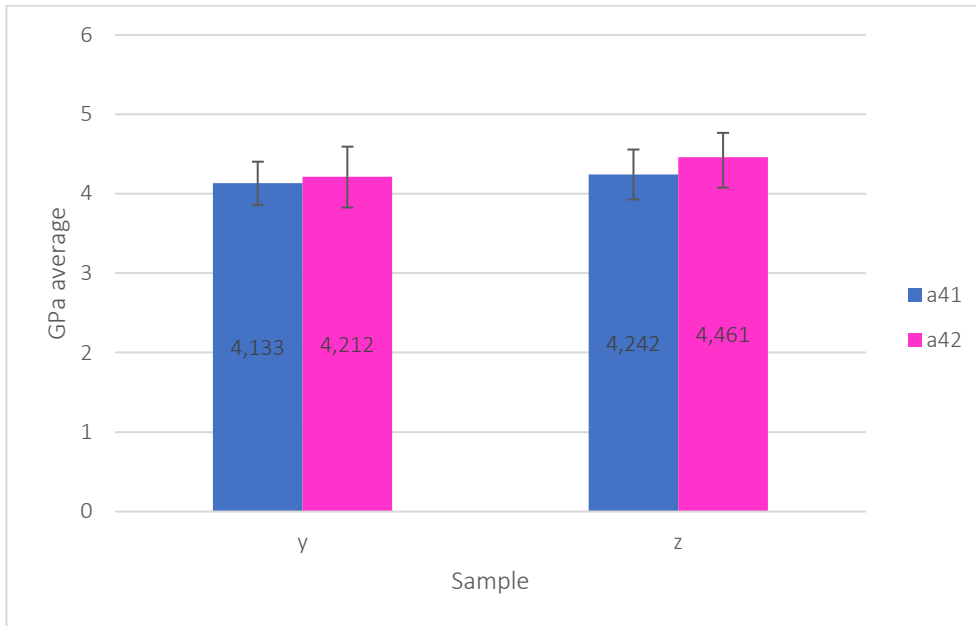


Figure 4.14: Berkovick results in y41-y42 and z41 and z42

So **Figure 4.14** showed no differences in hardness distribution regardless of building direction.

According to the work of Krystian Zyguła[40], HV1 in SLM and cast is 107 and 67.

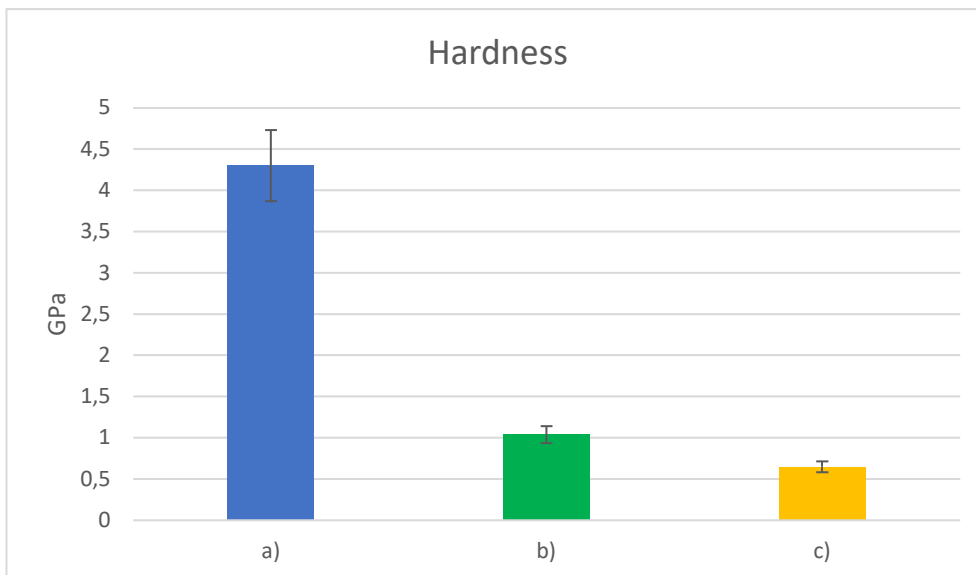


Figure 4.15: Hardness in GPa of a) SLM anodized b) SLM c) cast AlSi10Mg

Comparing SLM anodized, SLM and casting for the same AlSi10Mg is possible to observe that oxide hardness is 4 times greater than a no-anodized sample made with the same procedure. SLM process also has 60% higher hardness than cast material.

The difference between a cast material and the SLM alloy is due to the finer microstructure created during rapid solidification after laser melting.

The wear rate of anodized samples in XY direction is $0.98 \times 10^{-5} \pm 0.02 \times 10^{-5}$ mm³/(N mm).

Figure 4.16 showed not a smooth track, which is due to possible adhesive wear.

For higher magnifications, cracks close to the track are noticed as the response of the wear mechanism [41] (**Figure 4.17**)

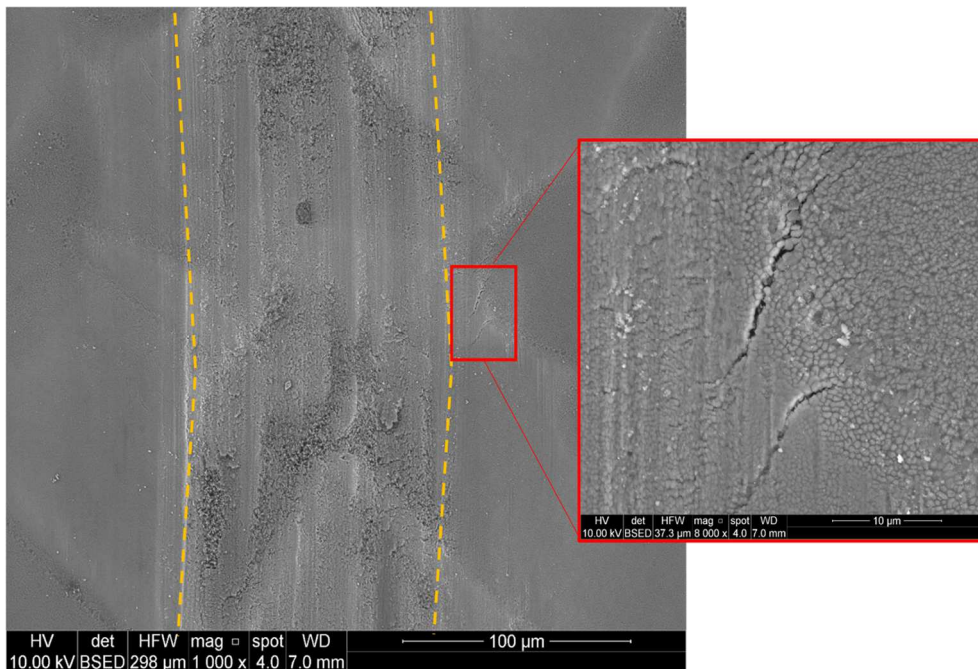


Figure 4.16: BSED wear track with adhesion phenomena and some lateral surface cracks

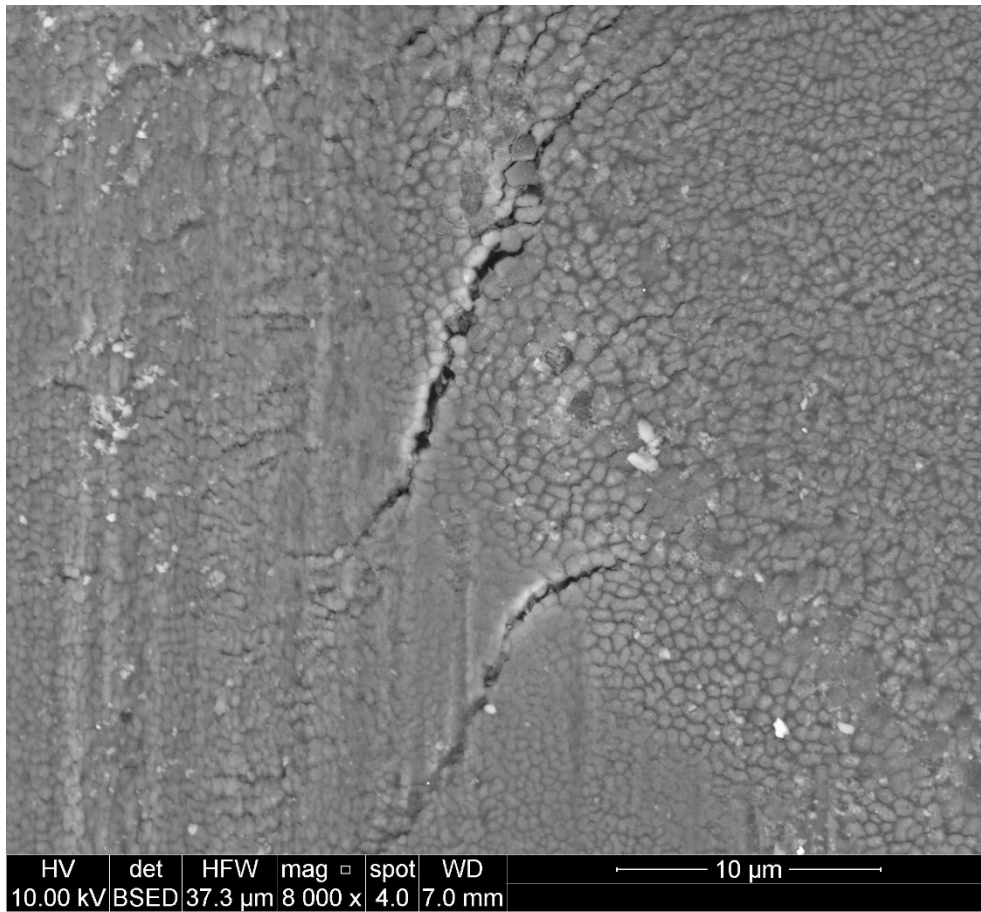


Figure 4.17: Lateral cracks due the wear test, close to the spin ball track

A faster removal material is the result of the presence of porosities which increase contact stress due to the lower loading area, and also, they increase the possibility of oxide delamination and crack propagation due to the obstacle of the compact growth of the oxide layer [42].

During trials, only the oxide layer wore out. With higher magnification with BDES, the substrate slightly glimpses (**Figure 4.18**).

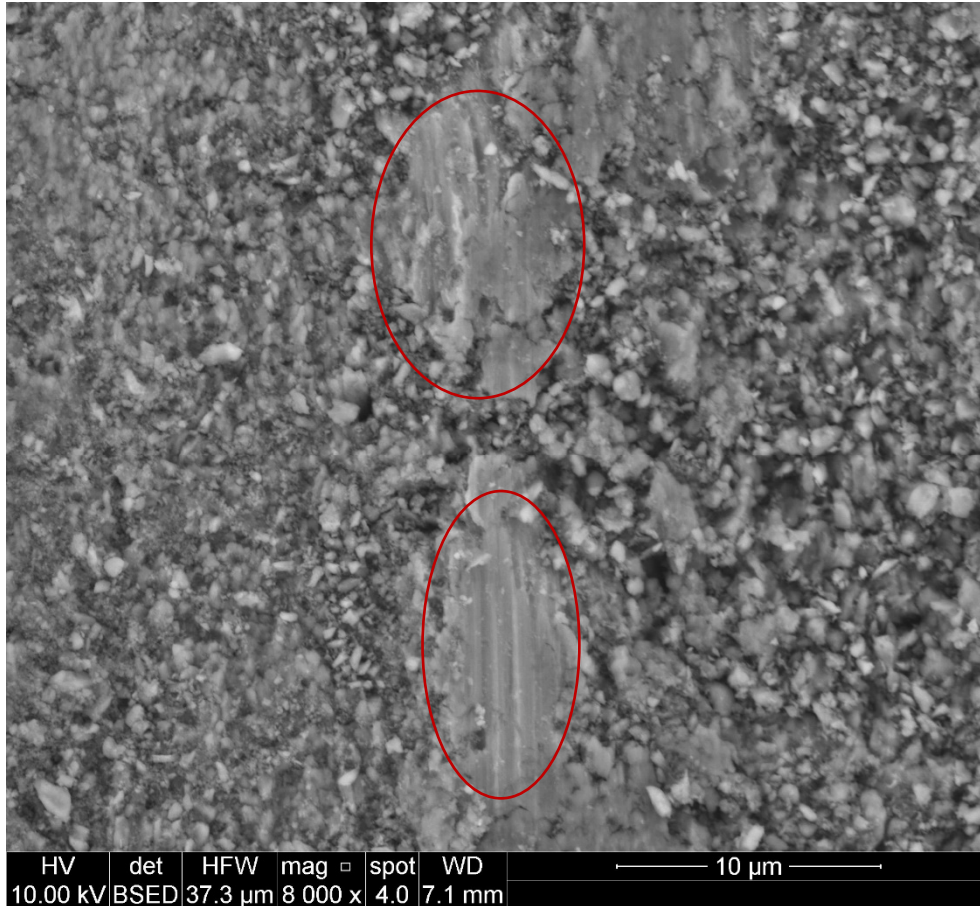


Figure 4.18: Glimpsed substrate after wear test

4.3. Corrosion tests

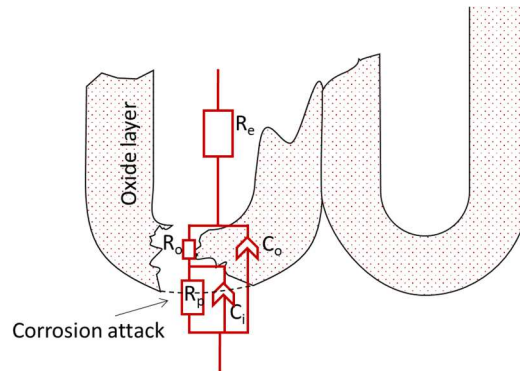
Samples are immersed in the corrosive solution for 24 hours (9 cycles of 3 hours each):

	<i>Cycle 1</i>	<i>Cycle 2</i>	<i>Cycle 3</i>	<i>Cycle 4</i>	<i>Cycle 5</i>	<i>Cycle 6</i>	<i>Cycle 7</i>	<i>Cycle 8</i>	<i>Cycle 9</i>
<i>za1</i>	23/04 14:02:22	23/04 17:09:36	23/04 20:15:45	23/04 23:23:38	24/04 02:30:10	24/04 05:41:50	24/04 08:53:39	24/04 11:59:37	24/04 14:13:32
<i>ya1</i>	24/04 14:55:54	24/04 18:02:48	24/04 21:09:13	25/04 00:16:50	25/04 03:24:27	25/04 06:32:05	25/04 09:38:55	25/04 12:46:33	25/04 16:00:10
<i>za2</i>	26/04 11:29:20	26/04 14:36:22	26/04 17:42:15	26/04 20:48:16	27/04 23:54:16	27/04 03:00:22	27/04 06:06:23	27/04 09:15:01	27/04 12:21:18
<i>za3</i>	27/04 13:18:38	27/04 16:26:25	27/04 19:33:24	27/04 22:40:53	28/04 01:47:05	28/04 04:53:23	28/04 07:59:58	28/04 11:05:55	28/04 14:11:54
<i>ya2</i>	01/05 11:13:38	01/05 14:26:16	01/05 17:33:38	01/05 20:40:34	01/05 23:47:08	02/05 02:53:23	02/05 05:59:29	02/05 09:05:19	02/05 12:11:13
<i>ya3</i>	02/05 13:07:32	02/05 16:14:26	02/05 19:27:21	02/05 22:34:58	03/05 01:41:32	03/05 04:48:20	03/05 07:54:29	03/05 11:00:44	03/05 14:10:12

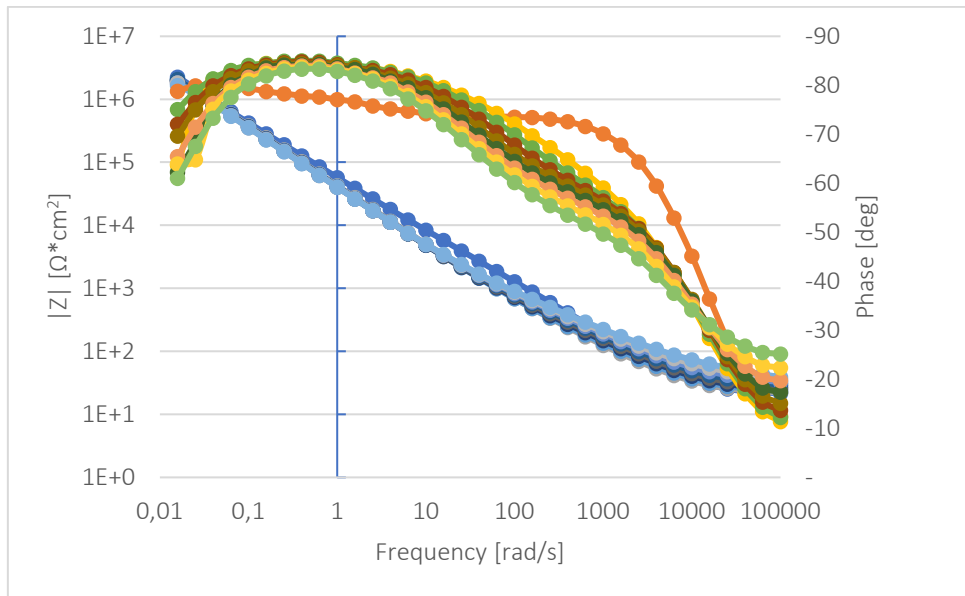
Table 4.3: Corrosion time cycle

Using ZSimple software, the best fitting (considering $\chi^2 \approx 10^{-4}$, as suggested in the literature) is the $\text{Re}(\text{Co}(\text{Ro}(\text{CiRp})))$.

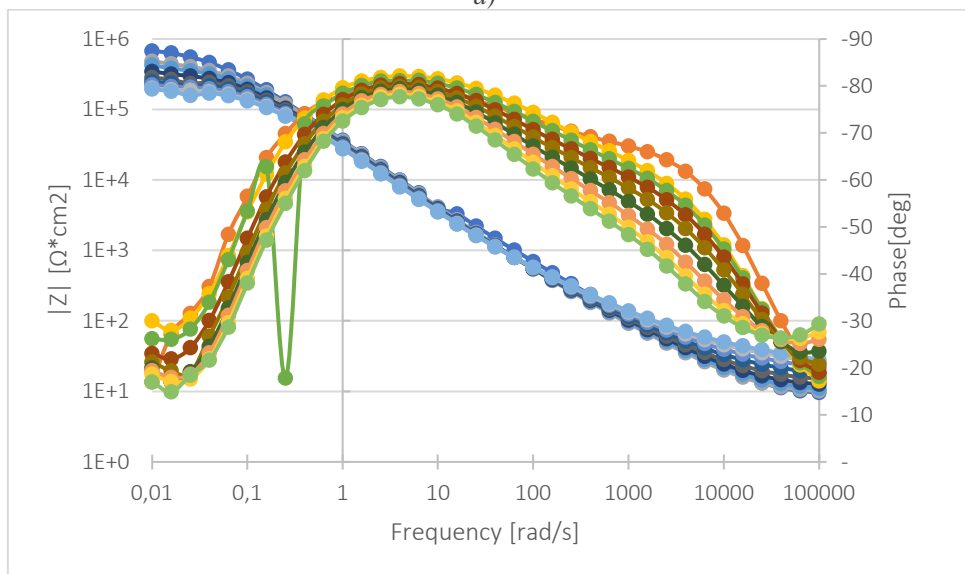
$$\text{Re}(\text{Co}(\text{Ro}(\text{CiRp})))$$



During immersion time phase angle increase and the total impedance modulus ($|Z|$) decrease (**Figure 4.19**)



a)



b)

Figure 4.19: Magnitude and phase of a) Y_a and b) Z_a ; in blue the phase; in green-yellow, the modulus

During this time, the decreasing value of the resistance R_p (**Figure 4.20**) indicates the destruction of the oxide layer and the consequent corrosion attack.

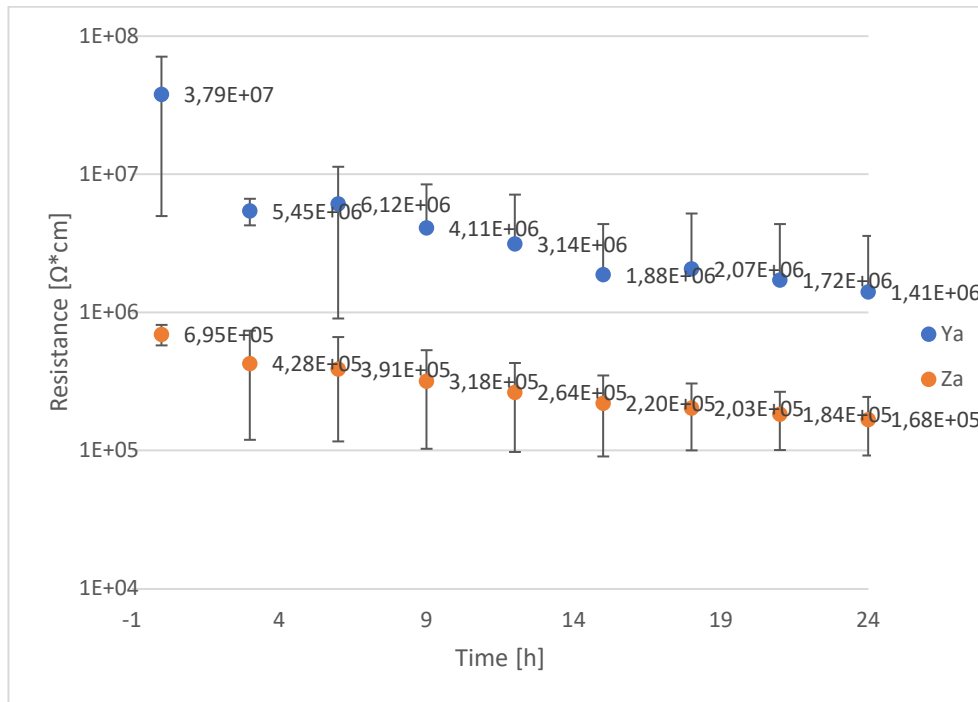


Figure 4.20: Evolution of the R_p of Ya and Za samples during the immersion time

To obtain more information about microstructure during corrosion and anodizing was applied a STEM analysis, for example, in Ya1 with a scale of 100 μm (**Figure 4.21**). The scenario seems quite similar to a no-anodized sample (**Figure 3.1**), but paying more attention is possible to notice the presence of some cracks in the surface.

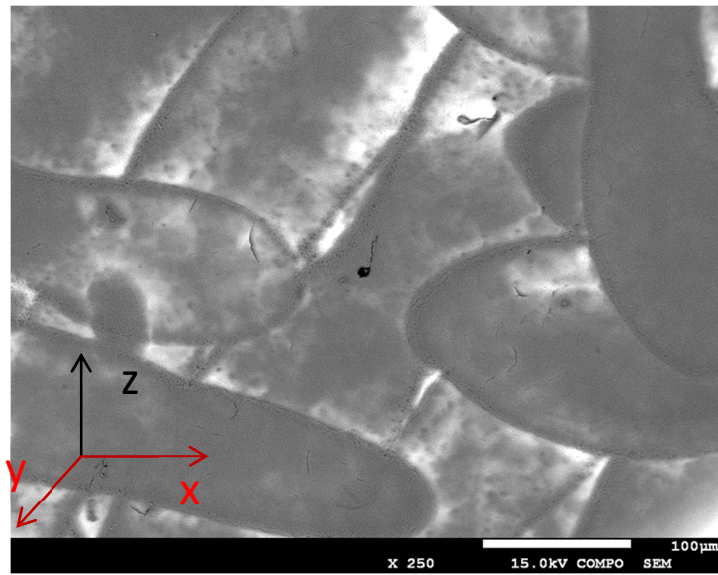


Figure 4.21: SEM of a parallel direction after EIS

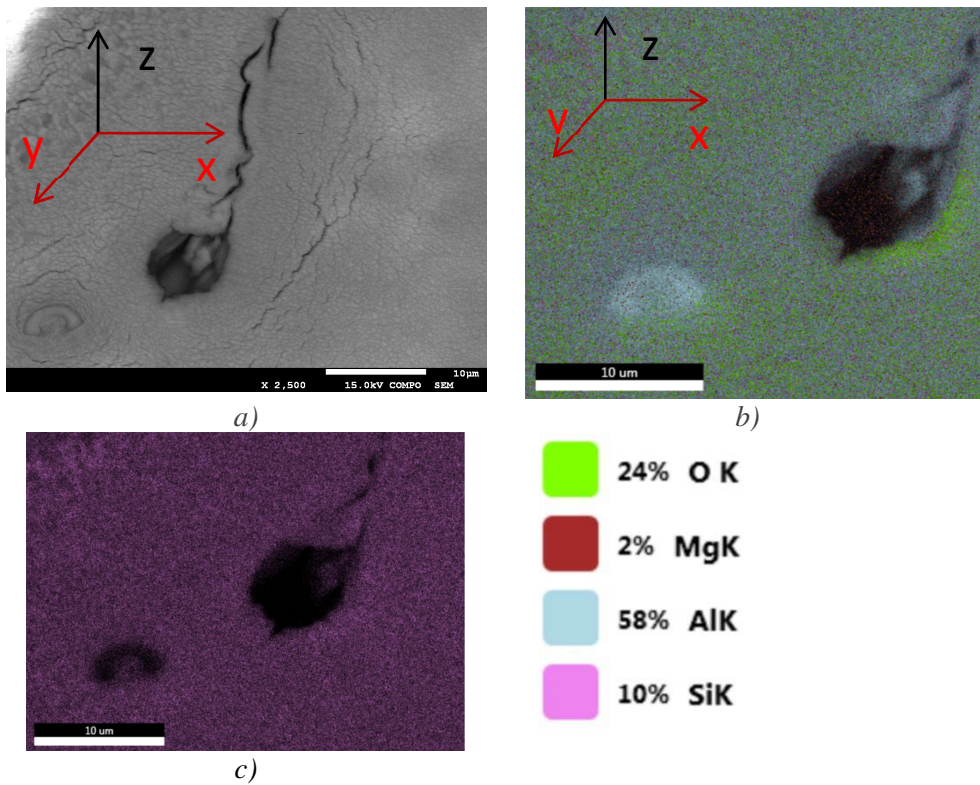


Figure 4.22: Detail of Ya1 a) and EDS of it b) c)

EDS for **Figure 4.22** gave results confirming the presence of the oxide (the O) with his voids and cracks.

Some spots of pure Al are still present. But Si remains uniform. (**Figure 4.22 c)**)

Using the same colours legend, Ya2 detects a spot with pure Si (**Figure 4.23 b)**):

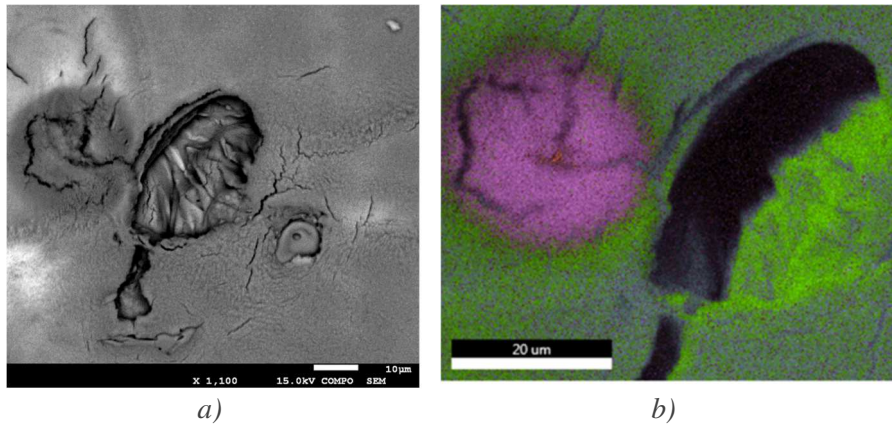


Figure 4.23: EDXAS mapping of the pitting corrosion on the Ya2 sample

In **Figure 4.23** corrosion attack penetrated the oxide layer and generated a corrosion pitting.

Same ongoings for Za1 as visible in **Figure 4.24**:

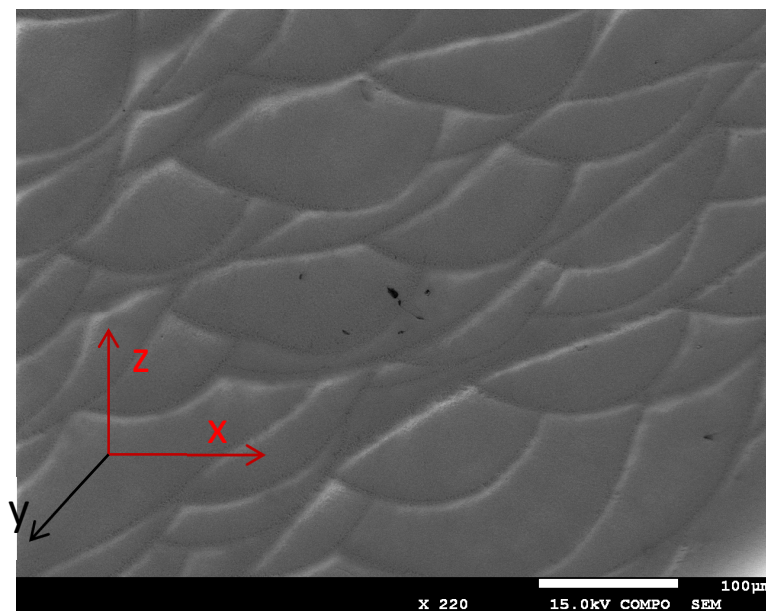


Figure 4.24: Perpendicular side (Za1) after EIS

Figure 4.24 shows a typical structure of SLM in 010 Miller' index, but also, in this case, is quite visible a defect.

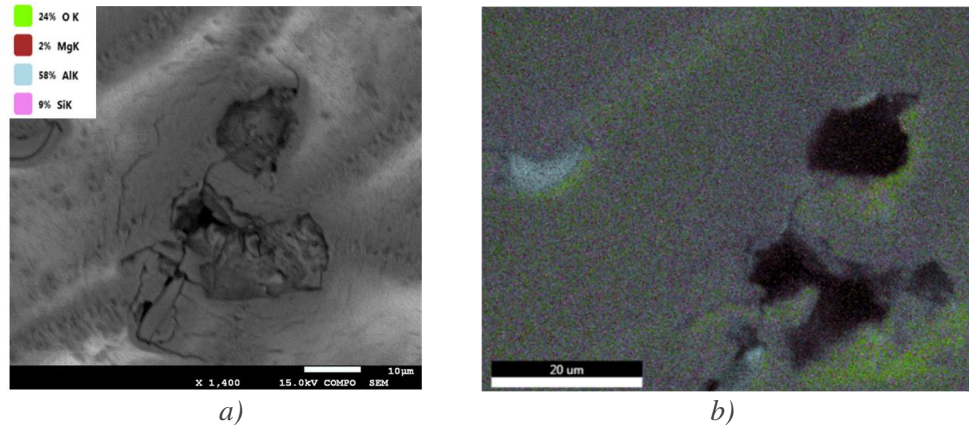


Figure 4.25: Detail of Zr1 after EIS a) and the element composition b)

In Figure 4.25 b) is quite evident the presence of the oxide layer and in a) also cracks are pretty detectable.

On both sides, it is possible still observe the porosity (dark spots) and the presence of pure particles due to the SLM process (can justify the presence of pure Al or Si); the existence of a high concentration of O can also be the result of previous oxidation (during the melting work of laser beam).

During anodizing, the oxide growth is homogeneously and relatively compact (visible also demonstrated in the measures conducted before and cross-section above); with a scanning transmission electron microscope, some cracks are pretty detectable. This is due to the creation of Si-O (oxygen presence in the images before is indicated with green colour) during the anodizing process that reacts slower than Al oxide. Silicon particles can also act as a shield to the Al above, and the presence of those Si particles can create volume expansions and create cracks and voids (justifying also **Figure 4.23** and **4.24**).

With the cross-section, it is also possible to observe the cracks and voids (before analysed just in top view) in a lateral section (**Figure 4.26**).

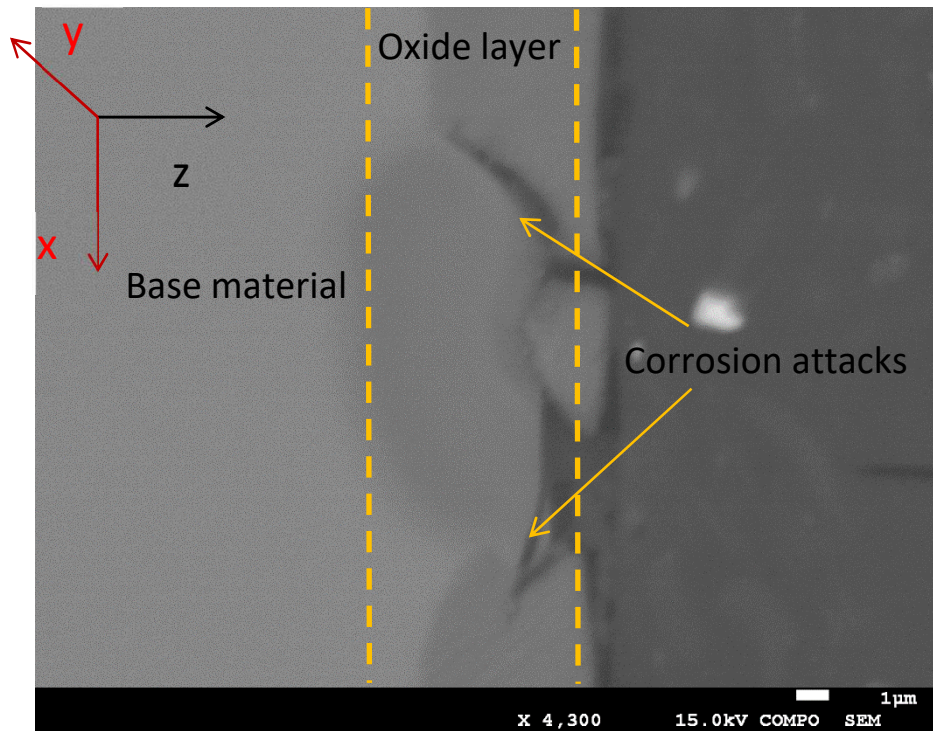


Figure 4.26: Cross section after anodization and corrosion attack

The **Figure 4.26** shows the presence of a crack in the oxide layer. With SEM, it is also quite clear to observe the O element. By the way, no traces of NaCl are available because of the proper cleaning of the samples after the corrosion process.

5. Conclusions

This work investigated the behaviour of the treatment of the anodizing process of AlSi10Mg alloy produced by selective laser melting.

The main results can be summarized as follow:

- The 3D-printed Al-alloy has an easily recognizable structure. The initial characterization by optical microscopy is possible to observe laser tracks. An elongated shape on the surface parallels the building platform and a semicircular shape on the perpendicular surface.
- The microstructure of melt pool borders is coarser (coarser Si network, eutectic phase and large Al cells) because of the lower cooling rate compared to the cooling rate at the centre of the melt pools.
- After anodizing, a tinner oxide layer was detected in the surfaces parallel to the building platform due to the homogenous microstructure of the pools; here, the oxide front has a higher probability of encountering Si and thus, the oxide layer front is more obstructed in this microstructure.
Due to the impurities, cracks and voids are visible during the oxide formation. The same alloy but casted has a thicker and less homogenous oxide layer than the additive because of not a proper spread of Si concentration.
- The oxide layer improves the hardness of the substrate by around four times more. It is higher in components of AM compared to the

conventional cast because of the change of microstructure due to the higher solidification rate.

- The wear rate calculated on the oxide layer generated on the surfaces parallel to the building direction is slightly above 10^{-5} mm³/(N mm). Also, for alloys produced by AM is possible to observe classical wear mechanisms, such as adhesive phenomena and cracks close to the wear track.
- The equivalent circuit that fits better the corrosive condition is the $Re(Co(Ro(CiRp)))$. During this time, it is possible to observe a decrease in the resistance (R_p) which indicates the destruction of anodic pores. Images also show corrosion pittings in correspondence with cracks and voids.

Acknowledgements

The thesis work was achieved within the framework of the Erasmus+ traineeship project and the collaboration between DTG-Università di Padova and HTK-Jonkoping University.

Bibliography

- [1] P. Wei *et al.*, "The AlSi10Mg samples produced by selective laser melting: single track, densification, microstructure and mechanical behavior," *Appl Surf Sci*, vol. 408, pp. 38–50, Jun. 2017, doi: 10.1016/j.apsusc.2017.02.215.
- [2] K. G. Prashanth *et al.*, "Microstructure and mechanical properties of Al-12Si produced by selective laser melting: Effect of heat treatment," *Materials Science and Engineering A*, vol. 590, pp. 153–160, Jan. 2014, doi: 10.1016/j.msea.2013.10.023.
- [3] E. Brandl, U. Heckenberger, V. Holzinger, and D. Buchbinder, "Additive manufactured AlSi10Mg samples using Selective Laser Melting (SLM): Microstructure, high cycle fatigue, and fracture behavior," *Mater Des*, vol. 34, pp. 159–169, Feb. 2012, doi: 10.1016/j.matdes.2011.07.067.
- [4] Law, "https://www.iso.org/standard/69669.html," 2020. <https://www.iso.org/standard/69669.html> (accessed Oct. 27, 2022).
- [5] E. Fella, "Selective Laser Beam Melting of AlSi10Mg Alloy," Politecnico di Milano, Milano, 2015.
- [6] "www.3Dhubs.com," Jun. 2019. www.3Dhubs.com (accessed Mar. 07, 2019).
- [7] "3D Printing Metal End-use Part Applications," 2019. <https://3dprint.com/252271/3d-printing-metal-end-use-part-applications/> (accessed Aug. 01, 2019).
- [8] A. H. Maamoun, Y. F. Xue, M. A. Elbestawi, and S. C. Veldhuis, "The effect of selective laser melting process parameters on the microstructure and mechanical properties of Al6061 and AlSi10Mg alloys," *Materials*, vol. 12, no. 1, Dec. 2018, doi: 10.3390/ma12010012.
- [9] C. Galy, E. le Guen, E. Lacoste, and C. Arvieu, "Main defects observed in aluminum alloy parts produced by SLM: From causes to consequences," *Additive Manufacturing*, vol. 22, Elsevier B.V., pp. 165–175, Aug. 01, 2018. doi: 10.1016/j.addma.2018.05.005.
- [10] J. Campbell, "Review of fluidity concepts in casting," *Cast Metals*, vol. 7, no. 4, pp. 227–237.
- [11] "www.european_alluminum.eu," Jun. 2019. www.european_alluminum.eu (accessed Oct. 27, 2019).

- [12] D. Verkens, "Study of the anodizing behaviour of additive manufactured AlSi10Mg aluminium alloy," Bruxelles, 2016.
- [13] Q. Yan, B. Song, and Shi J, "Microstructure and mechanical properties of Al-Mg-Mn-Er-Zr alloys fabricated by laser powder bed fusion," *Mater. Sci. Technol.*, vol. 41, pp. 199–208, 2020.
- [14] K. J. Moremi, H. Moller, and M. Khodja, "Comparative Study Of Additively Manufactured AlSi10Mg And Maraging M300 Steel Thin Walled Structures," Pretoria, 2018.
- [15] C. Weingarten, D. Buchbinder, N. Pircha, W. Meiners, K. Wissenbach, and R. Poprawe, "Formation and reduction of hydrogen porosity during selective laser melting of AlSi10Mg," *Journal of Materials Processing Tech*, Feb. 2015.
- [16] G. Timelli, *Innovation in metallurgical production*, vol. 2. Università degli Studi di Padova, 2019.
- [17] M. Fousova, D. Dvorsky, M. Vronka, D. Vojtech, and P. Lejcek, "The use of selective laser melting to increase the performance of AlSi9Cu3Fe alloy," *Materials*, vol. 11, no. 10, Oct. 2018, doi: 10.3390/ma11101918.
- [18] D. Agius, Kyriakos, Kourousis, and C. Wallbrink, "A Review of the As-Built SLM Ti-6Al-4V Mechanical Properties towards Achieving Fatigue Resistant Designs," *Metals (Basel)*, Jan. 2018.
- [19] B. Zhu, "On the Influence of Si on Anodising and Mechanical Properties of Cast Aluminium Alloys," Thesis, 2017. [Online]. Available: www.ju.se
- [20] W. Li *et al.*, "Effect of heat treatment on AlSi10Mg alloy fabricated by selective laser melting: Microstructure evolution, mechanical properties and fracture mechanism," *Materials Science and Engineering A*, vol. 663, pp. 116–125, Apr. 2016, doi: 10.1016/j.msea.2016.03.088.
- [21] T. Rubben, R. I. Revilla, and I. de Graeve, "Effect of Heat Treatments on the Anodizing Behavior of Additive Manufactured AlSi10Mg," *J Electrochem Soc*, vol. 166, no. 2, pp. C42–C48, 2019, doi: 10.1149/2.0371902jes.
- [22] X. Liu, C. Zhao, X. Zhou, Z. Shen, and W. Liu, "Microstructure of selective laser melted AlSi10Mg alloy," *Mater Des*, vol. 168, Apr. 2019, doi: 10.1016/j.matdes.2019.107677.
- [23] L. Yiwen *et al.*, "Preparation of Aluminum Nanomesh Thin Films from an Anodic Aluminum Oxide Template as Transparent Conductive Electrodes," vol. 6, no. 20114, 2016.

- [24] "Aluminum Anodizing," 2022. <https://electro-polish.com/processes/aluminum-anodizing/> (accessed Oct. 27, 2022).
- [25] L. Yuanjing *et al.*, "A Highly Controllable Electrochemical Anodization Process to Fabricate Porous Anodic Aluminum Oxide Membranes," *Lin et al. Nanoscale*, 2015.
- [26] J. M. Runge, *The Metallurgy of Anodizing Aluminum*. Chicago, IL, USA: Springer International Publishing, 2018.
- [27] P. Møller and L.P. Nielsen, *Advanced surface technology*. NASF, 2013.
- [28] B. Zhu, C. Zanella, R. Ambat, and Tekniska Högskolan. Högskolan i Jönköping, *Casting and anodising of Al alloys- Alloy design, manufacturing process and material properties*.
- [29] "Masterclass: Anodising titanium with Mooro cycles," 2022. <https://cyclingtips.com/2018/10/masterclass-anodising-titanium-with-mooro-cycles/> (accessed Oct. 27, 2022).
- [30] F. Bonollo, "Applicazioni industriali metallurgiche," *Università degli Studi di Padova*. 2018.
- [31] C. Zanella, "Functional material and surface," *Jönköping University*. Jönköping, 2019.
- [32] "Coating thickness measurement," 2019. <http://www.fischer-technology.com/en/united-states/knowledge/methods/coating-thickness-measurement/eddy-current-method-amplitude-sensitive/> (accessed Apr. 10, 2019).
- [33] I. Rosenthal, A. Stern, and N. Frage, "Microstructure and Mechanical Properties of AlSi10Mg Parts Produced by the Laser Beam Additive Manufacturing (AM) Technology," *Metallography, Microstructure, and Analysis*, vol. 3, no. 6, pp. 448–453, Dec. 2014, doi: 10.1007/s13632-014-0168-y.
- [34] I. Bouabibsa, S. Lamri, and F. Sanchette, "Structure, Mechanical and Tribological Properties of Me-Doped Diamond-Like Carbon (DLC) (Me = Al, Ti, or Nb) Hydrogenated Amorphous Carbon Coatings," *Coatings*, vol. 8, no. 10, p. 370, 2018, Accessed: Oct. 28, 2022. [Online]. Available: <https://doi.org/10.3390/coatings8100370>
- [35] R. I. Revilla *et al.*, "Galvanostatic Anodizing of Additive Manufactured Al-Si10-Mg Alloy," *J Electrochem Soc*, vol. 164, no. 14, pp. C1027–C1034, 2017, doi: 10.1149/2.1121714jes.

- [36] D. D. Gu, W. Meiners, K. Wissenbach, and R. Poprawe, "Laser additive manufacturing of metallic components: Materials, processes and mechanisms," *International Materials Reviews*, vol. 57, no. 3, pp. 133–164, May 2012, doi: 10.1179/1743280411Y.0000000014.
- [37] L. E. Fratila-Apachitei, J. Duszczyk, and L. Katgerman, "Vickers microhardness of AlSi(Cu) anodic oxide layers formed in H₂SO₄ at low temperature," 2003.
- [38] C. Weingarten, D. Buchbinder, N. Pirch, W. Meiners, K. Wissenbach, and R. Poprawe, "Formation and reduction of hydrogen porosity during selective laser melting of AlSi10Mg," *J Mater Process Technol*, vol. 221, pp. 112–120, Jul. 2015, doi: 10.1016/j.jmatprotec.2015.02.013.
- [39] L. Girelli *et al.*, "Evaluation of the impact behaviour of AlSi10Mg alloy produced using laser additive manufacturing."
- [40] K. Zyguła, H. Pasiowiec, B. Nosek, and N. Szysiak, "Mechanical properties and microstructure of AlSi10Mg alloy obtained by casting and SLM technique," 2018, [Online]. Available: www.worldscientificnews.com
- [41] A.-E. Jiménez and M.-D. Bermúdez, "Friction and wear," in *Tribology for Engineers*, Elsevier, 2011, pp. 33–63. doi: 10.1533/9780857091444.33.
- [42] P. Tonolini, L. Montesano, M. Tocci, A. Pola, and M. Gelfi, "Wear Behavior of AlSi10Mg Alloy Produced by Laser-Based Powder Bed Fusion and Gravity Casting," *Adv Eng Mater*, vol. 23, no. 10, Oct. 2021, doi: 10.1002/adem.202100147.

Appendix

<i>SLM XY</i>	<i>SLM XZ</i>	<i>Cast alloy</i>
0.108±0.02	0.12±0.01	0.37±0.03

Table 4.2: Oxide growth rate during anodizing of specimens (in H2SO4 electrolyte) in $\mu\text{m}/\text{min}$ [12]

